KeAi

CHINESE ROOTS
GLOBAL IMPACT

Contents lists available at ScienceDirect

# Petroleum Science

journal homepage: www.keaipublishing.com/en/journals/petroleum-science



# Original Paper

# SeisResoDiff: Seismic resolution enhancement based on a diffusion model



Hao-Ran Zhang <sup>a, b</sup>, Yang Liu <sup>a, b, c, \*</sup>, Yu-Hang Sun <sup>d</sup>, Gui Chen <sup>a, b</sup>

- <sup>a</sup> State Key Laboratory of Petroleum Resources and Engineering, China University of Petroleum (Beijing), Beijing, 102249, China
- <sup>b</sup> CNPC Key Laboratory of Geophysical Prospecting, China University of Petroleum (Beijing), Beijing, 102249, China
- <sup>c</sup> School of Petroleum, China University of Petroleum (Beijing) at Karamay, Karamay, 834000, Xinjiang, China
- <sup>d</sup> Northeast Petroleum University, Daqing, 163318, Heilongjiang, China

## ARTICLE INFO

## Article history: Received 13 March 2024 Received in revised form 4 June 2024 Accepted 1 July 2024 Available online 6 July 2024

Edited by Meng-Jiao Zhou

Keywords:
Seismic resolution enhancement
Diffusion model
High resolution
Reservoir characterization
Deep learning
Seismic data processing

## ABSTRACT

High resolution of post-stack seismic data assists in better interpretation of subsurface structures as well as high accuracy of impedance inversion. Therefore, geophysicists consistently strive to acquire higher resolution seismic images in petroleum exploration. Although there have been successful applications of conventional signal processing and machine learning for post-stack seismic resolution enhancement, there is limited reference to the seismic applications of the recent emergence and rapid development of generative artificial intelligence. Hence, we propose to apply diffusion models, among the most popular generative models, to enhance seismic resolution. Specifically, we apply the classic diffusion model—denoising diffusion probabilistic model (DDPM), conditioned on the seismic data in low resolution, to reconstruct corresponding high-resolution images. Herein the entire scheme is referred to as SeisResoDiff. To provide a comprehensive and clear understanding of SeisResoDiff, we introduce the basic theories of diffusion models and detail the optimization objective's derivation with the aid of diagrams and algorithms. For implementation, we first propose a practical workflow to acquire abundant training data based on the generated pseudo-wells. Subsequently, we apply the trained model to both synthetic and field datasets, evaluating the results in three aspects: the appearance of seismic sections and slices in the time domain, frequency spectra, and comparisons with the synthetic data using real well-logging data at the well locations. The results demonstrate not only effective seismic resolution enhancement, but also additional denoising by the diffusion model. Experimental comparisons indicate that training the model on noisy data, which are more realistic, outperforms training on clean data. The proposed scheme demonstrates superiority over some conventional methods in high-resolution reconstruction and denoising ability, yielding more competitive results compared to our previous research.

© 2024 The Authors. Publishing services by Elsevier B.V. on behalf of KeAi Communications Co. Ltd. This is an open access article under the CC BY-NC-ND license (http://creativecommons.org/licenses/by-nc-nd/4.0/).

## 1. Introduction

Exploration seismology plays an extremely important role in petroleum industry to determine the distribution of reservoirs and guide the location of well drilling by providing the images of subsurface structures. Seismic images with high resolution are helpful for interpreting the geologic structures precisely, and inverting for subsurface physical properties accurately (Yilmaz, 2001). However, due to the stratum absorption effect during the seismic wave

propagation as well as some limits in seismic acquisition and data processing, constraining the band-width of signals or damage some frequencies that benefit high resolution, people sometimes cannot obtain seismic data with satisfied resolution. Therefore, resolution enhancement has always been a hot topic in seismic exploration.

For post-stack (or migration) seismic data that are the results of seismic processing procedures and ready for the subsequent interpretation tasks, high resolution generally means good distinction of thin layers underground in a seismic section and broad band of signals in the spectrum. Many approaches have been proposed to extend the band-width of seismic data as the objective for resolution enhancement. These approaches can be divided into two aspects in general: conventional ways, and deep-learning-

<sup>\*</sup> Corresponding author. State Key Laboratory of Petroleum Resources and Engineering, China University of Petroleum (Beijing), Beijing, 102249, China. *E-mail address*: wliuyang@vip.sina.com (Y. Liu).

based methods.

Among the conventional ways, deconvolution, which compresses the seismic wavelet to approximate reflectivity based on seismic convolution theory (Robinson, 1967), has become a type of the most commonly used methods (Cao and Yuan, 2016). There have been a few classic methods including least-squares inverse filtering (Berkhout, 1977), Wiener spiking deconvolution (Leinbach, 1995), predictive deconvolution (Peacock and Treitel, 1969), surface-consistent deconvolution (Levin, 1989), etc. Developed from the deconvolution, some new methods based on the sparsity assumption of the reflectivity have been proposed and successfully applied, constituting the sparse-spike deconvolution (SSD) or the sparse-spike inversion (SSI) (Taylor et al., 1979; Levy and Fullagar, 1981; Sacchi, 1997; Puryear and Castagna, 2008; Velis, 2008; Zhang and Castagna, 2011; Gholami and Sacchi, 2012; Kazemi and Sacchi, 2014; Ma et al., 2017; Li et al., 2021). To compensate the attenuation on high frequencies caused by the stratum absorption effect, inverse-Q filtering (Hale, 1981; Hargreaves and Calvert, 1991; Wang, 2002, 2006; Margrave et al., 2011) under the constant-Q theory (Kjartansson, 1979), becomes another critical technology, and has been applying to both pre- and post-stack data (Yao et al., 2003; Zhang and Ulrych, 2007; Li et al., 2015; Zhang et al., 2015). Considering the wavelet variation in time and space (nonstationary situation), some researchers have recovered frequencies with Garbor transform (Margrave, 1998; Margrave et al., 2011; Gao et al., 2009; Wang et al., 2013), S transform (Stockwell et al., 1996; Zhou et al., 2014; Lin et al., 2022), and empirical mode decomposition (Huang et al., 1998; Dragomiretskiy and Zosso, 2014; Chen et al., 2022c: Cao et al., 2023). Some other approaches that invert for reflectivity in complicated cases (e.g. non-stationary signals, noisy data, and blind deconvolution) have been developed as well (Chai et al., 2014; Chen et al., 2019, 2022b; Jiang et al., 2021). The conventional approaches mentioned above have been demonstrated to be effective and applied widely in resolution enhancement, but those methods have limitations as well. For instance, some of the methods have their own assumptions towards seismic data or the subsurface properties, such as the sparsity assumption of the reflectivity in SSI. Some methods rely on the elaborate design of the algorithms involving massive expertise, experience, and manipulation of experimental setups.

Deep learning has been increasingly attracting attention in exploration geophysics in which automation and intelligence are highly valued (Harsuko and Alkhalifah, 2022; Cheng and Alkhalifah, 2023). There are many successful deep learning applications in solving seismic problems, such as data denoising and reconstruction with self-supervised learning (Zhang et al., 2019b; Zhang and Liu, 2022; Chen et al., 2022a; Birnie and Alkhalifah, 2022; Liu et al., 2023b; Chen and Liu, 2024), wavefield extrapolation and simulations with Fourier neural operators (Song and Wang, 2022; Grady et al., 2023), full waveform inversion (FWI) (Sun and Demanet, 2020; Li et al., 2023; Alali and Alkhalifah, 2023; Yang et al., 2023b; Wang et al., 2023a), seismic impedance as well as amplitude variation with offset (AVO) inversion (Zhang et al., 2022a, 2022b; Sun and Liu, 2022; Sun et al., 2024), and geological structure segmentation (Wu et al., 2019; Zhang et al., 2021; Yang et al., 2024). Applying deep learning techniques in seismic resolution enhancement is certainly without exception. In view of the similarities between seismic sections and natural images, the ideas from image super-resolution in computer vision problems can be borrowed for improving seismic resolution (Li et al., 2022; Sun et al., 2022; Hamida et al., 2023; Min et al., 2023; Lin et al., 2023; Zeng et al., 2023). Nonetheless, the resolution degradation in seismic data is not identical with that in natural images, and seismic resolution enhancement is a comprehensive change for the signals including amplitude and phase adjustments. Combining the

conventional algorithms with deep learning is a good way to exploit the advantages from both. To this end, some parts in the conventional algorithms can be substituted by neural networks that are able to build complex mappings between data and provide prior information to the reflectivity inversion (Chen et al., 2021a, 2021b, 2023; Gao et al., 2022b; Xu et al., 2022). Generalization of the networks is a big issue when we train networks on a dataset which has different features from the data that we apply to in the inference stage. Therefore, the structure and the facies constrains can be added into the deep learning applications (Li et al., 2022; Hamida et al., 2023; Gao et al., 2023; Wang et al., 2023b). In addition, using well logging as auxiliary information to build training datasets (Choi et al., 2021; Gao et al., 2023; Guo et al., 2023) or adopting domain adaptation methods (Zhang et al., 2023) is effective for the generalization improvement.

Among deep learning algorithms, generative models have shown promising abilities of generating data subject to the distribution learned from the given data. Generative adversarial network (GAN) (Goodfellow et al., 2014) becomes a representative of this type of models. Zhang et al. (2019a) used high resolution data processed by a conventional method as labels to train a GAN. Oliveira et al. (2019), Sun et al. (2022), and Lin et al. (2023) improved the seismic resolution by GANs in an image superresolution way which conducts seismic section interpolation and reconstruction. To ensure more reasonable generated high resolution results and good generalization of the networks, some scholars use CycleGANs in the resolution enhancement task with adding structure constrains (Gao et al., 2022a) and weakly supervised learning (Liu et al., 2023a). However, there are difficulties in training GANs, specifically, when trying to find a proper set of hyper-parameters and decide the balanced weights between different loss functions to make the training stable (Arjovsky and Bottou, 2017; Pan et al., 2020; Wang et al., 2023c). Diffusion models become one of the state-of-the-art deep generative models at present, showing superb performance with flexibility and huge potential in a variety of fields (Dhariwal and Nichol, 2021; Saharia et al., 2022; Yang et al., 2023a). Diffusion models avoid training a discriminator like in a GAN and just learn the reverse of simple forward diffusion process. The application of diffusion models in geophysics is emerging but still at an early stage, in which the diffusion models are mostly used in seismic denoising and data reconstruction. For example, Peng et al. (2024) applied a denoising diffusion probabilistic model (DDPM) (Ho et al., 2020) to the strong random noise attenuation. The initial DDPM and some other versions of diffusion models such as denoising diffusion implicit model (DDIM) (Song et al., 2021a) are used for shot gather interpolation (Hou et al., 2023; Deng et al., 2024; Wei et al., 2023; Liu and Ma, 2024). Durall et al. (2023) apply a conditioned DDPM (Sohn et al., 2015; Saharia et al., 2023) to eliminating multiples from seismic data in addition to random noise attenuation and data interpolation. There are a few applications on other topics. Wang et al. (2023a) trained a diffusion model which offers prior subsurface knowledge as a regularizer to improve the performance of the conventional FWI process. Jiang et al. (2023) applied a conditional DDPM to a geological structure identification task. Nevertheless, there has not been a reference about diffusion-model application on seismic resolution enhancement so far. In this paper, we implement a preliminary test on this task.

We introduce a scheme in which we apply a conditional diffusion model that combines the classic DDPM with low-resolution seismic images as prior conditions to enhance seismic resolution. Firstly, we present the theories of diffusion models and derive the optimization objective. The derivation of this objective shows significant differences from other deep-learning-based methods. Following this, we propose a workflow to generate pseudo-wells

and simulate geological models based on features from target field data, ensuring the availability of sufficient training data. To bolster the reliability of predictions, we incorporate diverse noisy data for network training. Experiments using both synthetic and field datasets are conducted to validate the feasibility and efficacy of the proposed scheme. The promising predicted results reveal the considerable potential of diffusion-model-based applications for seismic resolution enhancement.

## 2. Resolution enhancement with a diffusion model

The basic theory of diffusion models includes diffusion and denoising processes, as shown in Fig. 1. The training of the diffusion models contains both of the processes, while only the denoising process is conducted in the inference stage. The details are illustrated in the subsections below. Specifically, the procedures of the method are illustrated in the subsection "Training and inference".

## 2.1. Diffusion (forward process)

Diffusion is a process adding Gaussian random noise to a piece of given clean data step by step, until the clean data become pure Gaussian noise ultimately. This process looks like molecular diffusion in thermodynamics which inspires the name of diffusion models. As illustrated in Fig. 1, the diffusion process which reflects the posterior  $q(\mathbf{x}_{1:T}|\mathbf{x}_0)$  can be formed through a Markov chain with adding noise to the original seismic data  $\mathbf{x}_0$  over T steps:

$$q(\mathbf{x}_{1:T}|\mathbf{x}_0) := \prod_{t=1}^{T} q(\mathbf{x}_t|\mathbf{x}_{t-1})$$
 (1)

where  $q(\mathbf{x}_t|\mathbf{x}_{t-1})$  represents the conditional distribution of the data  $\mathbf{x}_t$  at step t given  $\mathbf{x}_{t-1}$  at previous step t-1, and ":=" indicates "define as".

To make the diffusion controllable, following Ho et al. (2020) and Luo (2022), normal distribution is chosen for this process. The data  $\mathbf{x}_t$  can be obtained through  $\mathbf{x}_{t-1}$  by adding the noise  $\epsilon$  sampled from a standard normal distribution  $\mathcal{N}(\mathbf{0}, \mathbf{I})$ :

$$\mathbf{x}_{t} = \sqrt{1 - \beta_{t}} \mathbf{x}_{t-1} + \sqrt{\beta_{t}} \epsilon, \quad \epsilon \sim \mathcal{N}(\mathbf{0}, \mathbf{I})$$
 (2)

where  $\beta_t$  in our work is the designated hyper-parameter at step t and increases as t goes from 0 to T, subject to  $0 < \beta_t < 1$ . Then,  $q(\mathbf{x}_t | \mathbf{x}_{t-1})$  can be written as

$$q(\mathbf{x}_{t}|\mathbf{x}_{t-1}) := \mathcal{N}\left(\mathbf{x}_{t}; \sqrt{1 - \beta_{t}} \,\mathbf{x}_{t-1}, \beta_{t} \mathbf{I}\right)$$
(3)

with  $\sqrt{1-\beta_t}\mathbf{x}_{t-1}$  as the mean and  $\beta_t$  as the variance in this

Gaussian distribution.

Further, according to the property of Gaussian distribution, combining the Eqs. (1) and (3), one can derive the probability distribution of the data  $\mathbf{x}_t$  at any step t given the original clean data  $\mathbf{x}_0$ :

$$q(\mathbf{x}_t|\mathbf{x}_0) = \mathcal{N}\left(\mathbf{x}_t; \sqrt{\alpha_t} \mathbf{x}_0, (1 - \alpha_t)\mathbf{I}\right)$$
(4)

i.e.

$$\mathbf{x}_{t} = \sqrt{\alpha_{t}} \mathbf{x}_{0} + \sqrt{1 - \alpha_{t}} \epsilon, \quad \epsilon \sim \mathcal{N}(\mathbf{0}, \mathbf{I})$$
 (5)

where  $\alpha_t := 1 - \beta_t$  and  $\alpha_t := \prod_{i=1}^t \alpha_i$ .

## 2.2. Denoising (reverse process)

Literally, denoising process removes the noise from the beginning pure Gaussian noise  $\mathbf{x}_{t-T}$  and reconstructs data  $\mathbf{x}_{t-1}$  step by step until the desired  $\mathbf{x}_0$ , which is the clean seismic dataset in high resolution in our research. As the reverse of the aforementioned diffusion process  $q(\mathbf{x}_t|\mathbf{x}_{t-1})$ , denoising can be denoted as  $q(\mathbf{x}_{t-1}|\mathbf{x}_t)$ . If  $\beta_t$  is small enough,  $q(\mathbf{x}_{t-1}|\mathbf{x}_t)$  satisfies a Gaussian distribution as well (Feller, 1949). However, it is impossible to deduce the exact posterior  $q(\mathbf{x}_{t-1}|\mathbf{x}_t)$  in reality because there are numerous possibilities when one samples noise from a normal distribution in the diffusion process. In practice, the reverse process is performed by a network (denoted by the distribution  $p_{\theta}(\mathbf{x}_{0:T})$  with network weights  $\theta$  an transitions in another Markov chain, starting at the given noise  $p(\mathbf{x}_T) = \mathcal{N}(\mathbf{x}_T; \mathbf{0}, \mathbf{I})$ :

$$\begin{aligned} p_{\theta}(\mathbf{x}_{0:T}) &:= p(\mathbf{x}_T) \prod_{t=1}^T p_{\theta}(\mathbf{x}_{t-1} | \mathbf{x}_t) \\ p_{\theta}(\mathbf{x}_{t-1} | \mathbf{x}_t) &:= \mathcal{N}(\mathbf{x}_{t-1}; \mu_{\theta}(\mathbf{x}_t, t), \sigma_{\theta}(\mathbf{x}_t, t)) \end{aligned} \tag{6}$$

where  $p_{\theta}(\mathbf{x}_{t-1}|\mathbf{x}_t)$  represents a single step in the reverse process with shared network weights  $\theta$  across steps, as shown in Fig. 1. To that end, the objective of network training is to learn a distribution  $p_{\theta}$  consistent with the distribution q.

# 2.3. Optimization of the reverse process

Based on the analysis above, the reverse process that gives us expected high resolution results is an optimization problem, in which the learnable distribution  $p_{\theta}$  is forced to be similar to the reverse of the diffusion process q. It is natural to use Kullback-Leibler (KL) divergence (Kullback and Leibler, 1951)  $D_{\text{KL}}(q \parallel p_{\theta})$  for the distance measurement between the two distributions. Then, the objective function can be formulated as

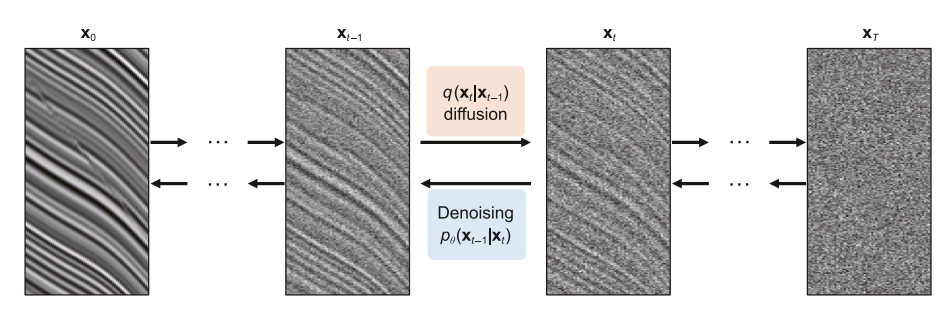


Fig. 1. Diagram of diffusion and denoising processes in diffusion models.

$$\begin{aligned} \underset{\theta}{\operatorname{argmin}} D_{KL}(q \parallel p_{\theta}) &= \underset{\theta}{\operatorname{argmin}} \sum_{i=1}^{m} q(x_{i}) \log \left( \frac{q(x_{i})}{p_{\theta}(x_{i})} \right) \\ &= \underset{\theta}{\operatorname{argmin}} \left( \sum_{i=1}^{m} q(x_{i}) \log q(x_{i}) - \sum_{i=1}^{m} q(x_{i}) \log p_{\theta}(x_{i}) \right) \\ &= \underset{\theta}{\operatorname{argmin}} \left( - \sum_{i=1}^{m} q(x_{i}) \log p_{\theta}(x_{i}) \right) (q \text{ is known}) \\ &= \underset{\theta}{\operatorname{argmin}} \mathbb{E}_{x \sim q(x)} [-\log p_{\theta}(x)] \text{ (Definition of expectation } \mathbb{E}) \end{aligned}$$

where the function "argmin" stands for "argument of the minimum" and herein outputs a set of network weights  $\theta$  that minimize  $D_{\mathrm{KL}}(q\|p_{\theta})$  over the domain of network weights, and q represents the diffusion which is already designated and nothing related to the network.

The derivation above reveals that the network optimization pursues a largest  $p_{\theta}$ . In particular, we need to obtain the largest probability for reconstructing the original seismic data  $\mathbf{x}_0$ . With the definition of expectation and KL divergence, Bayes rules, and the previous formulas as well as some algebraic manipulation, the optimization of the reverse process forces the neural network to predict noise as similar to Gaussian noise as possible. That is, the optimization objective of the reverse process during model training, is equivalent to the minimum of the difference between the network output and Gaussian noise:

$$\underset{\boldsymbol{\theta}}{\operatorname{argmin}} D_{\mathrm{KL}}(\boldsymbol{q} \parallel p_{\boldsymbol{\theta}}) \Leftrightarrow \\ \underset{\boldsymbol{\theta}}{\operatorname{argmin}} \|\widehat{\boldsymbol{\epsilon}}_{\boldsymbol{\theta}}(\mathbf{x}_{t}, t) - \boldsymbol{\epsilon}_{0}\|_{2}^{2}, \boldsymbol{\epsilon}_{0} \sim \mathcal{N}(\boldsymbol{\epsilon}; \mathbf{0}, \mathbf{I})$$
(8)

where the source Gaussian noise  $\epsilon_0$  determines seismic data  $\mathbf{x}_t$  at any step t from the original data  $\mathbf{x}_0$ , and  $\hat{\epsilon}_{\theta}(\mathbf{x}_t,t)$  represents the network prediction that approximates  $\epsilon_0$  when given the data  $\mathbf{x}_t$  at step t. We refer the readers to **Appendix A** for the detailed derivation of the optimization objective.

Once the network has the ability of predicting Gaussian noise (after network training), we are able to infer the data  $\mathbf{x}_{t-1}$  from  $\mathbf{x}_t$  based on Eq. (6) and appendix Eq. (A.10):

$$\begin{aligned} p_{\theta}(\mathbf{x}_{t-1}|\mathbf{x}_{t}) &= \mathcal{N}\Big(\mathbf{x}_{t-1}; \mu_{\theta}(\mathbf{x}_{t}, t), \tilde{\sigma}^{2}\mathbf{I}\Big) &\Leftrightarrow \\ \mathbf{x}_{t-1} &= \mu_{\theta}(\mathbf{x}_{t}, t) + \tilde{\sigma}\mathbf{z}, \mathbf{z} \sim \mathcal{N}(\mathbf{0}, \mathbf{I}) \\ &= \frac{1}{\sqrt{\alpha_{t}}} \left(\mathbf{x}_{t} - \frac{1 - \alpha_{t}}{\sqrt{1 - \overline{\alpha_{t}}}} \hat{\epsilon}_{\theta}(\mathbf{x}_{t}, t)\right) + \tilde{\sigma}\mathbf{z}, \mathbf{z} \sim \mathcal{N}(\mathbf{0}, \mathbf{I}) \end{aligned} \tag{9}$$

where the standard deviation  $\tilde{\sigma}$  is only the function of  $\alpha_t$  (appendix Eq. (A.6)) that is designated in advance during the diffusion process. In the formula above, we use the similar reparameterization of writing a normal distribution as in Eq. (2). The details about network training and inference are illustrated afterwards.

# 2.4. Conditional diffusion models

The purpose of our research is the reconstruction of high resolution seismic data from low resolved data. The network needs to learn the low-high resolution relationship in a supervised manner. Fortunately, diffusion models can be easily conditioned (Saharia et al., 2023; Durall et al., 2023), so that we are able to train the models with input-label data pairs.

We can give source-target (i.e. input-label) data pairs as the

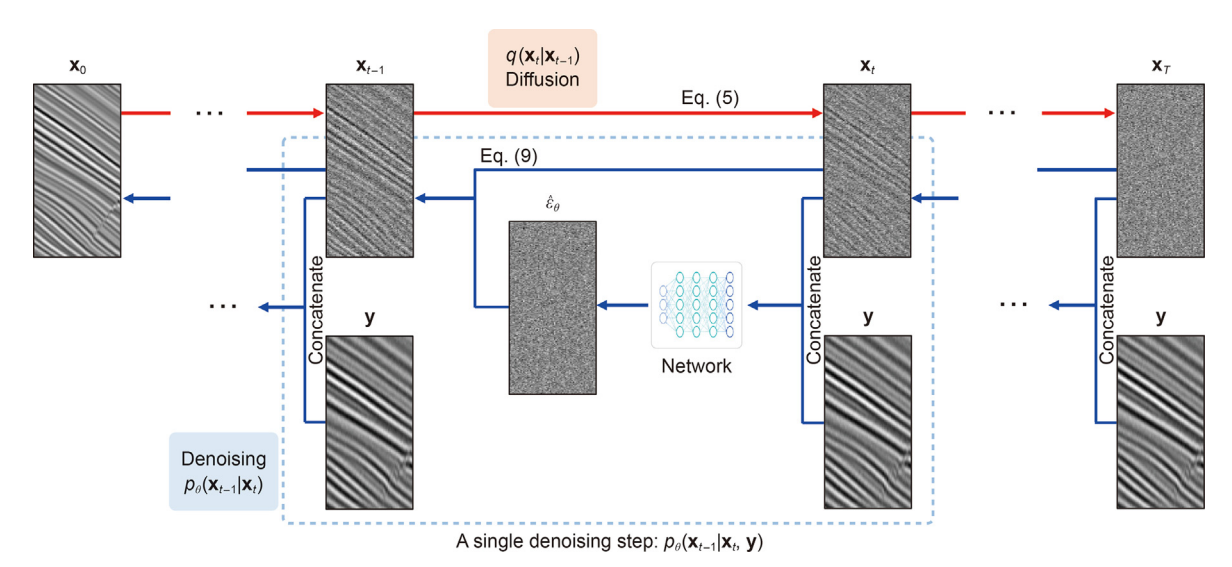


Fig. 2. Diagram of the proposed conditional diffusion model SeisResoDiff, in which the diffusion and denoising processes are depicted in red and blue arrows, respectively.

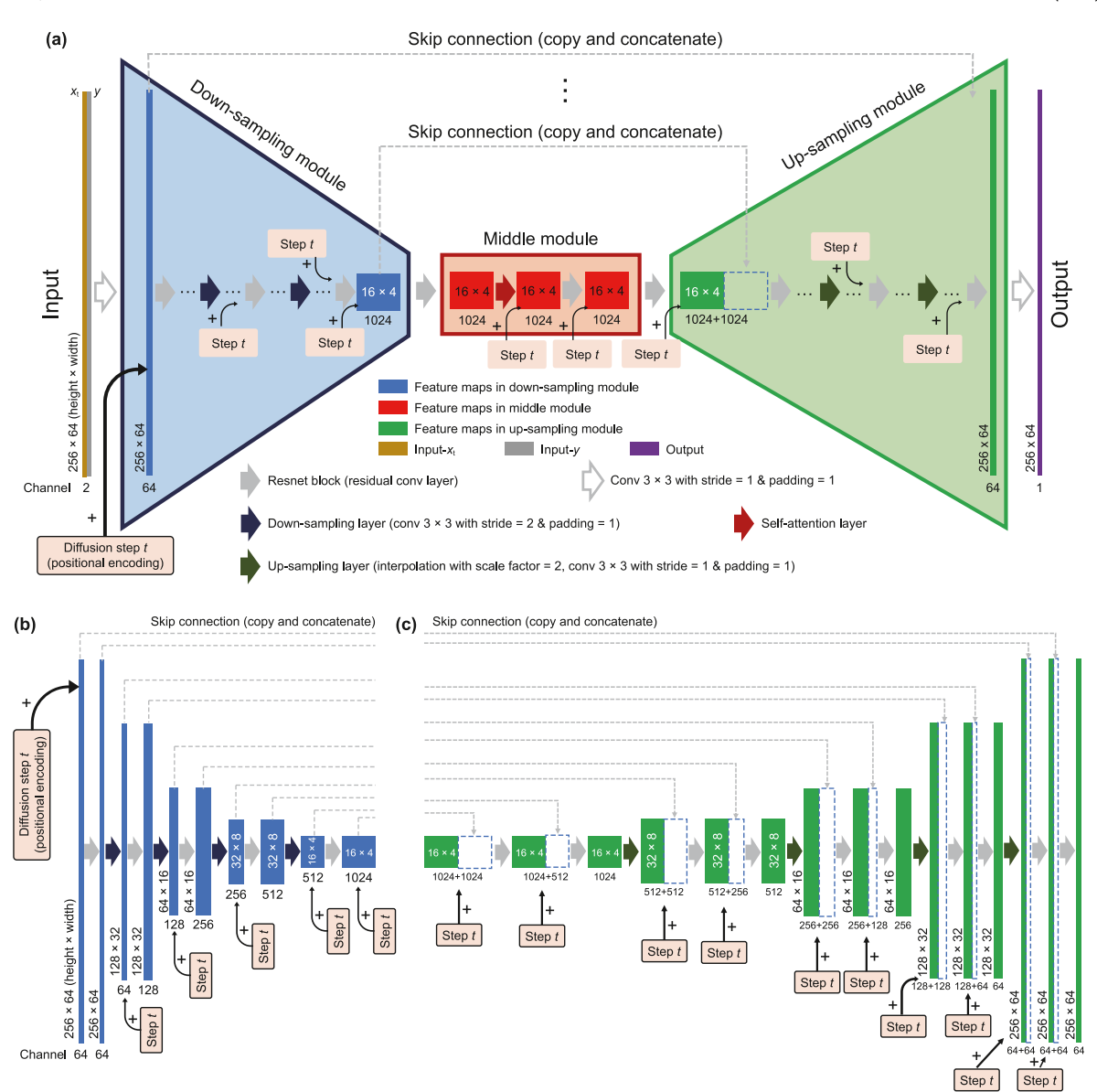


Fig. 3. The network architecture. (a) Overview of the network. (b) The details in down-sampling module. (c) The details in up-sampling module.

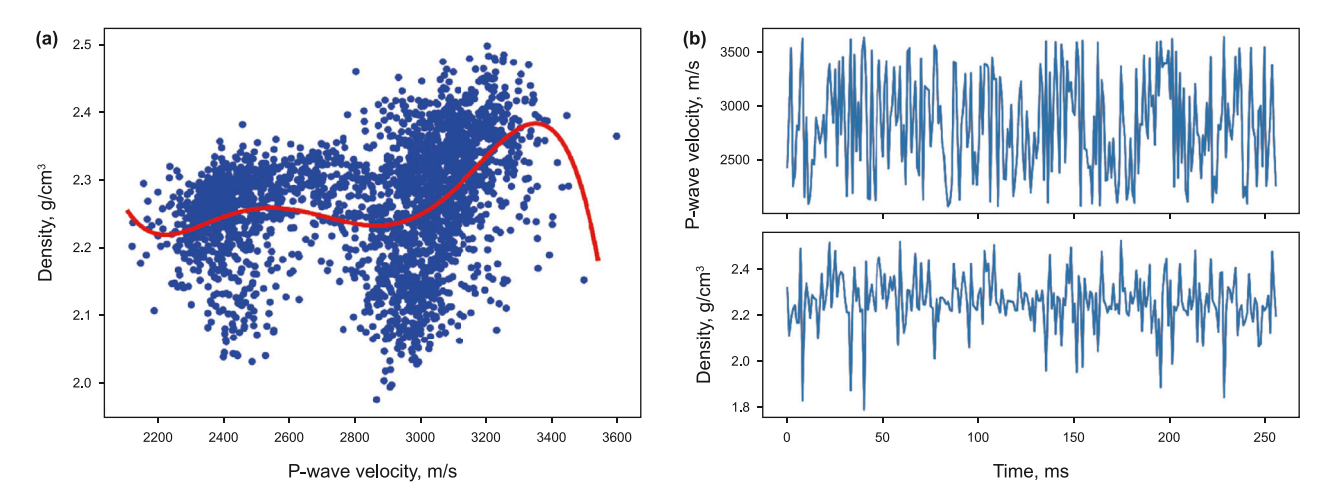


Fig. 4. Generation of pseudo-wells from data fitting. (a) The scatter plot as well as the fitting curve of rock density and P-wave velocity from well-logging. (b) A pseudo-well including rock density and P-wave velocity.

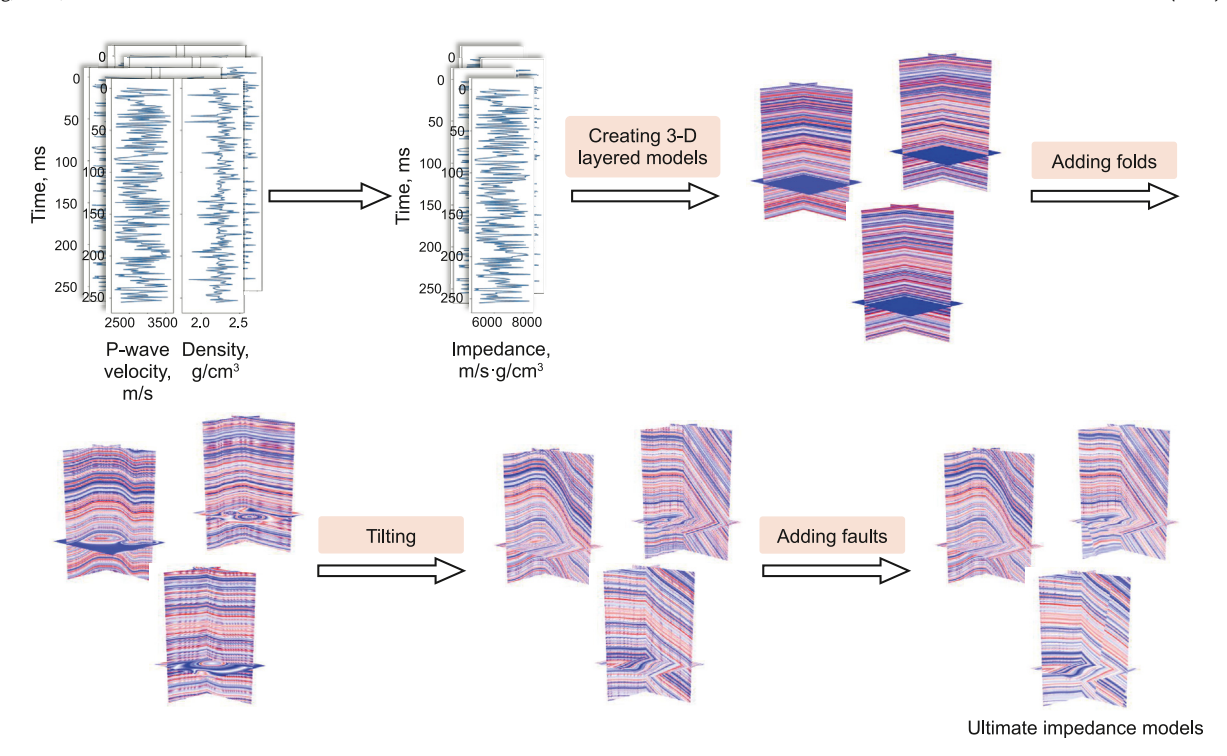


Fig. 5. Generation process of the 3-D impedance geological models with similar structural features to field seismic data using pseudo wells.

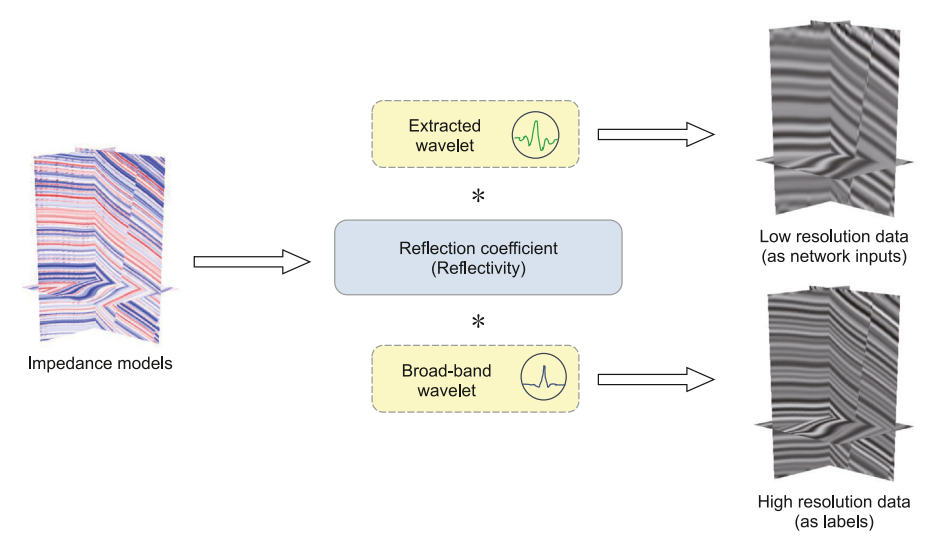


Fig. 6. Process of seismic data simulation based on impedance geological models.

samples drawn from a distribution  $p(\mathbf{x}|\mathbf{y})$ , in which  $\mathbf{y}$  and  $\mathbf{x}$  represent the source and target data, respectively. Conditional diffusion models are trained to map the source data  $\mathbf{y}$  into the target  $\mathbf{x}$  in a stochastic iterative refinement process that is defined above as the denoising process, i.e.  $p_{\theta}(\mathbf{x}_{t-1}|\mathbf{x}_t,\mathbf{y})$  such that  $\mathbf{x}_0 \sim p(\mathbf{x}|\mathbf{y})$ . For resolution enhancement, the diffusion model is conditioned on the seismic data in low resolution as the source data  $\mathbf{y}$ , and starts the refinement from pure Gaussian noise  $\mathbf{x}_T$  until the denoised seismic data in high resolution  $\mathbf{x}_0$ . In our practice, a piece of data  $\mathbf{x}_T$  sampled from the standard normal distribution is concatenated with a low resolved seismic data section  $\mathbf{y}$  as a part of the network inputs (whereas the other part is the step t). After training, the network is supposed to output Gaussian noise  $\hat{\epsilon}_{\theta}(\mathbf{x}_t,\mathbf{y},t)$ , and we can calculate

 $\mathbf{x}_{t-1}$  with Eq. (9) iteratively till the desired high resolution data  $\mathbf{x}_0$ . This section is depicted in Fig. 2.

## 2.5. Training and inference

Both of the diffusion and denoising processes are involved in the training stage. During every training iteration, each piece of target data  $\mathbf{x}_0$  within a batch is randomly assigned a forward diffusion step t to provide  $\mathbf{x}_t$  based on Eq. (5). Then,  $\mathbf{x}_t$  concatenated with the source data  $\mathbf{y}$  that are in low resolution, forming dual-channel data, are input into the network. The corresponding step t is embedded into a vector as a network input as well, using the positional encoding method from Chen et al. (2021c). The discrepancy

between the network output and the Gaussian noise sampled from  $\mathcal{N}(\mathbf{0}, \mathbf{I})$  is calculated to update the network according to Eq. (8) or appendix Eq. (A.11). We refer the readers to Algorithm 1 for the training details.

**Algorithm 1.** Training a network in the conditional diffusion model SeisResoDiff.

```
Input: T: Number of diffusion steps in the forward process:
y: Source data (low resolution); \mathbf{x}_0: Target data (high resolution, label);
Output: Trained diffusion model with network weights \theta;
1: Initialize: t \sim \text{Uniform}(1,T);
2: Initialize: \beta_t \sim \text{Uniform}(\beta_{-}\text{start}, \beta_{-}\text{end}), i.e. \beta_t = (\beta_{-}\text{end} - \beta_{-}\text{start})t/T;
3: while not converged do
4: (target, source) = (\mathbf{x}_0, \mathbf{y}) \sim q(\mathbf{x}_0, \mathbf{y});
      \alpha_t = 1 - \beta_t; \overline{\alpha}_t = \prod_{i=1}^t \alpha_i;
6:
      \epsilon \sim \mathcal{N}(\mathbf{0}, \mathbf{I});
7:
      \mathbf{x}_t = \sqrt{\overline{\alpha}_t} \mathbf{x}_0 + \sqrt{1 - \overline{\alpha}_t} \epsilon;
8: Compute the gradient w.r.t. the network weights \theta:
9: \nabla_{\theta} \| \widehat{\epsilon}_{\theta}(\mathbf{x}_{t}, \mathbf{y}, t) - \epsilon \|_{2}^{2}, i.e. \nabla_{\theta} \| \widehat{\epsilon}_{\theta}(\sqrt{\overline{\alpha}_{t}} \mathbf{x}_{0} + \sqrt{1 - \overline{\alpha}_{t}} \epsilon, \mathbf{y}, t) - \epsilon \|_{2}^{2};
10: Update network weights \theta;
```

In the inference stage, a step-wise denoising process from step T to 1 is conducted for providing the noise-free high resolution results. Similar to the reverse process in the training, the network gets the source data  $\mathbf{y}$  as well as  $\mathbf{x}_t$  as inputs, and predicts the noise  $\hat{\epsilon}_{\theta}(\mathbf{x}_{t},\mathbf{y},t)$ . As illustrated in the last subsection, the whole inference process starts from  $\mathbf{x}_T$  with the condition  $\mathbf{y}$ , and reconstructs the ultimate high resolution seismic data based on Eq. (9). We use the same hyper-parameters  $\beta_t$  as in the training. The detailed procedures are listed in Algorithm 2.

Algorithm 2. Inference of the conditional diffusion model SeisResoDiff.

#### 2.6. The network

In fact, excluding the network design, the conditional diffusion model can accept either 2-D or 3-D seismic data. The data shape depends on the network architecture, which is primarily influenced by the desired results and computational efficiency. In this work. we develop a 2-D network that takes 2-D seismic sections as input and outputs 2-D results to achieve high efficiency. We take the fundamental idea of U-net (Ronneberger et al., 2015), and use a network adjusted from classic works in diffusion models including Ho et al. (2020), Song et al. (2021b), and Saharia et al. (2023). Fig. 3 depicts the network architecture in detail. Note that the data size in both the seismic traces and time samples maintains same for both low-resolution inputs and high-resolution outputs.

## 3. Data preparation

Supervised learning needs plenty of labeled training data to train neural networks. However, generalization issue appears easily when there are prominent differences between the training and inference data. It is necessary to create training datasets as similar to the inference data as possible. We propose a workflow in which we can model the training data based on the features from a target field seismic survey. Taking the field data we use as an example, the data preparation steps are listed as follows.

(1) Fitting the relationship between P-wave velocity and rock density from well-logging. There are 11 wells in our target survey. All samples of the rock density (noted as  $\rho$ ) and Pwave veloctiy (noted as  $v_P$ ) from the 11 wells are shown in a scatter plot in Fig. 4(a). We take  $\rho$  as a function of  $\nu_P$ . The nonlinear relation of  $\rho$ - $v_P$  can be observed obviously. Inspired by the empirical relations in Brocher (2005), we employ quintic polynomial regression to fit the  $\rho$ - $\nu$ P relation and get the fitting function shown as below:

```
Input: T: Number of denoising steps in the reverse process, normally equals to that in the forward process; y: Source data (in low resolution);
Output: Denoised high resolution seismic data \mathbf{x}_0;
```

```
1: Initialize: \mathbf{x}_T \sim \mathcal{N}(\mathbf{0}, \mathbf{I});
```

11: end while

**3: Initialize:**  $\beta_t \sim \text{Uniform}(\beta_-\text{start}, \beta_-\text{end})$ , i.e.  $\beta_t = (\beta_-\text{end} - \beta_-\text{start})t/T$ ;

**4:** For t = T to 1, steplength = 1 do

5: 
$$\alpha_t = 1 - \beta_t$$
;  $\overline{\alpha}_t = \prod_{i=1}^t \alpha_i$ ;

6: 
$$\mathbf{z} \sim \mathcal{N}(\mathbf{0}, \mathbf{I})$$
 if  $t > 1$  else  $\mathbf{z} = \mathbf{0}$ ;

7: 
$$\mathbf{x}_{t-1} = \frac{1}{\sqrt{\alpha_t}} \left( \mathbf{x}_t - \frac{1 - \alpha_t}{\sqrt{1 - \overline{\alpha_t}}} \hat{\mathbf{e}}_{\theta}(\mathbf{x}_t, \mathbf{y}, t) \right) + \frac{(1 - \alpha_t)(1 - \overline{\alpha_{t-1}})}{1 - \overline{\alpha_t}} \mathbf{z}, \text{ i.e. Eq. (9)};$$

8: end for

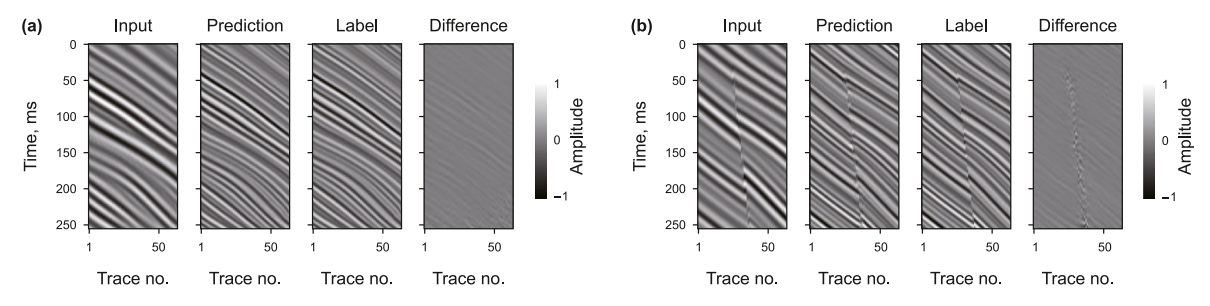


Fig. 7. SeisResoDiff inference results of two inline sections in the synthetic training dataset. The four images from left to right in each section exhibit the low resolution image as the conditional part of network inputs, the predicted high resolution result from the trained network, the high resolution label (ground truth), and the difference between the prediction and the label, respectively. (a) Training section-A. (b) Training section-B. 3172

**<sup>2:</sup> Initialize:**  $t \sim \text{Uniform}(1,T)$ ;

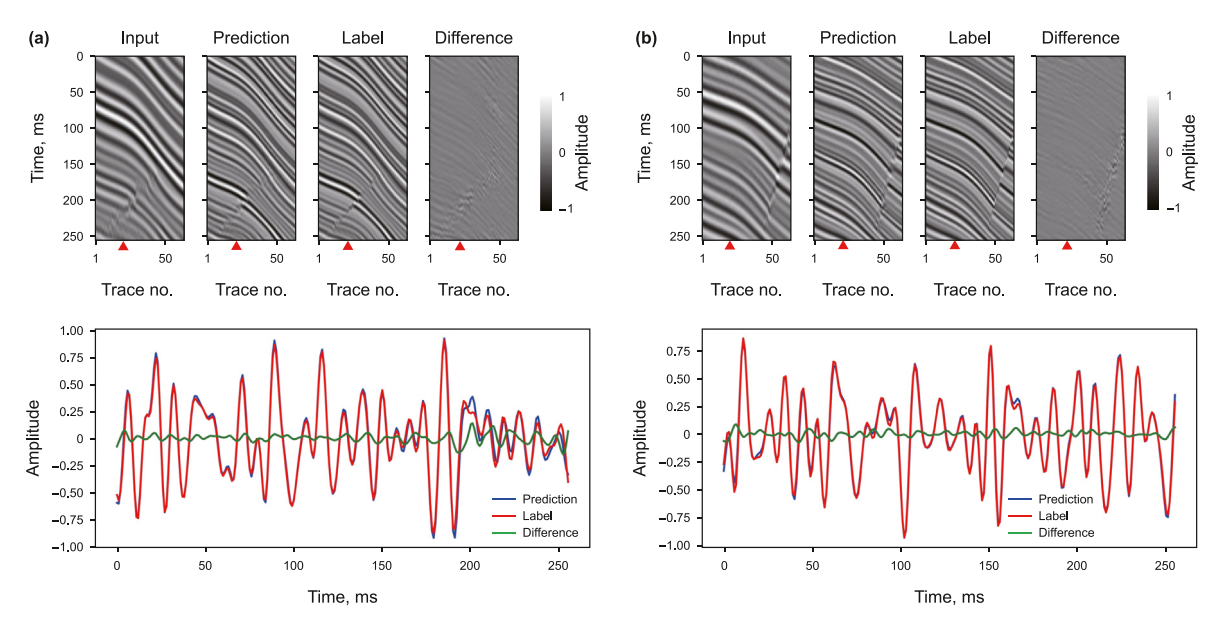
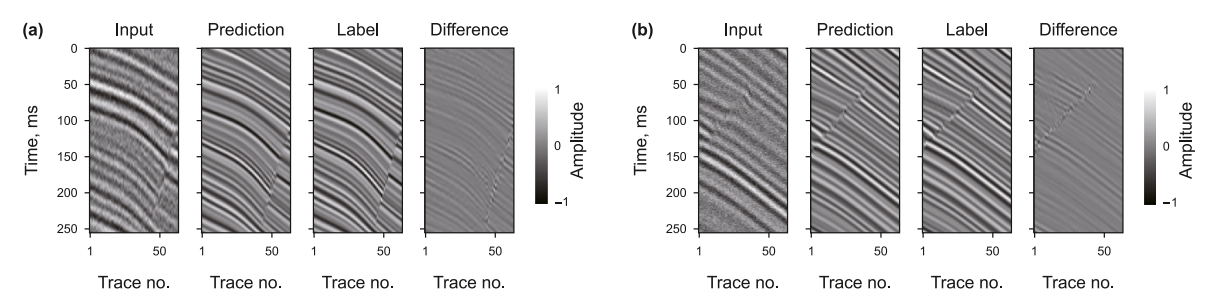
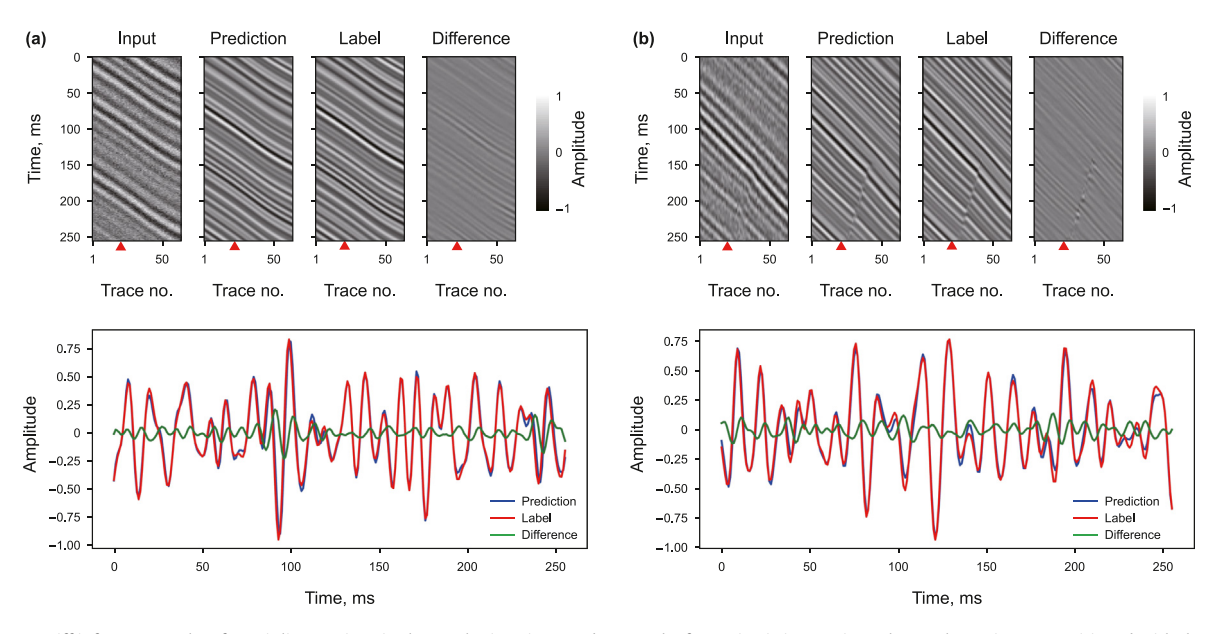


Fig. 8. SeisResoDiff inference results of two inline sections in the synthetic test dataset. The four seismic images in each sample section are positioned with the same layout as in Fig. 7. The curve plot below the seismic images in each subgraph displays the comparison between the network input and prediction for a randomly selected seismic trace at the location indicated by the red triangles on seismic images. (a) Test section-C. (b) Test section-D.



**Fig. 9.** SeisResoDiff inference results of two inline sections in the synthetic noisy training dataset. The four images from left to right in each section exhibit the noisy low resolution image as the conditional part of network inputs, the predicted high resolution result from the trained network, the high resolution label (ground truth), and the difference between the prediction and the label, respectively. **(a)** Training section-E. **(b)** Training section-F.



**Fig. 10.** SeisResoDiff inference results of two inline sections in the synthetic noisy test dataset. The four seismic images in each sample section are positioned with the same layout as in Fig. 9. The curve plot below the seismic images in each subgraph displays the comparison between the network input and prediction for a randomly selected seismic trace at the location indicated by the red triangles on seismic images. **(a)** Test section-G. **(b)** Test section-H.

$$\begin{split} \rho &= -3.077 \tilde{v}_P^5 + 42.231 \tilde{v}_P^4 - 230.1 \tilde{v}_P^3 + 622.125 \tilde{v}_P^2 - 834.748 \tilde{v}_P \\ &+ 446.949 \end{split}$$

where  $\tilde{v}_P = v_P/1000.0$ , under Système International d'Unités (SI). The fitting curve is plotted in red in Fig. 4(a). It is necessary to point out that the data fitting above can be completed even if there is only a single well. The more wells we have the more accurate data fitting we get.

- (2) Generating massive pseudo-wells according to the rock property fitting function. Since there are many possibilities to return a density when given a certain velocity, we also offer a range of density values along and neighboring to the fitting curve. That is, regarding to each sample of velocity, we are able to obtain a density sample randomly chosen from a range satisfied in Gaussian distribution, of which the mean value is located on the fitting curve. Velocity samples are randomly generated in a trend consistent with the general velocity increase trending in depth, but limited by the range on the actual wells. An example pseudo-well is shown in Fig. 4(b).
- (3) Creating an amount of geological models with similar structural features from the field data based on the pseudowells. Same as in our antecedent research (Zhang et al., 2023), we adopt the geologic modeling approach from Wu et al. (2020) to build subsurface models. Taking the product of the velocity and density from the pseudo-wells as impedance, we expand the impedance of each pseudo-well (1-D time series) to 3-D layered models by spreading impedance laterally. Then, for each layered model, we add tilting, folds, and faults in sequence to the model with different groups of parameters. By investigation on the field data, we constrain the dip angle of the layers changing in a small range as in the real case. Slight folds and few faults are controlled in the same reason. Finally, we obtain diverse geological models, some as shown in Fig. 5.
- (4) Modeling low and high resolution data based on the geological models. The reflectivity (also called reflection coefficients) of the models can be calculated by taking the

difference between the impedance values of upper and lower layers over the impedance sum of the two layers. Then, the reflectivities are convolved with two different seismic wavelets to simulate low (for network inputs) and high (as labels) resolution seismic data. We use a wavelet extracted from the field data for the low resolution synthetic data, whereas an expected broad-band wavelet for the labels. Fig. 6 shows a diagram of this step.

We present two experimental examples on synthetic and field data, respectively, in the following sections. In the former example, the synthetic dataset is divided into the training and inference datasets. The diffusion model is trained with the training dataset, and used in the inference both for the synthetic and field data examples to validate our approach. All of the field data are used for inference.

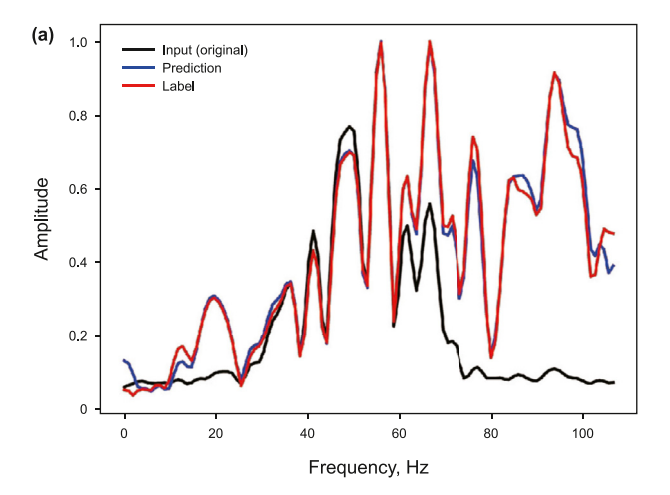
# 4. Synthetic data example

## 4.1. Performance in training and inference

Following the steps above, we acquire 220 geological models in three dimensions (81, 64, 256), representing (inline numbers, crossline numbers, time samples) for the experiments. Taking inline sections (in 2-D) as the data we test on, a half of all inline sections is randomly selected as the training data. A single random inline section chosen except for any training section from each model composes the test dataset.

To reach a balance between performance and efficiency, the conditional diffusion model is trained for 20000 iterations with batch size of 16 on an NVIDIA GeForce RTX 4090 GPU. The training is quite efficient, taking 2 h. We set the number of total diffusion steps as 2000 in our experiments. The inference conducts full 2000 steps for denoising, while in the training, the diffusion step t is assigned randomly for each piece of data to provide  $\mathbf{x}_t$  within a batch per iteration.

Fig. 7 shows some examples of the training results. In each row, the image at first column is in low resolution as the condition part of the network input. The second and third images show the ultimate output of the network and the labeled high resolution section, respectively. The last image shows the discrepancy between the network output and the label. We can observe the stable training



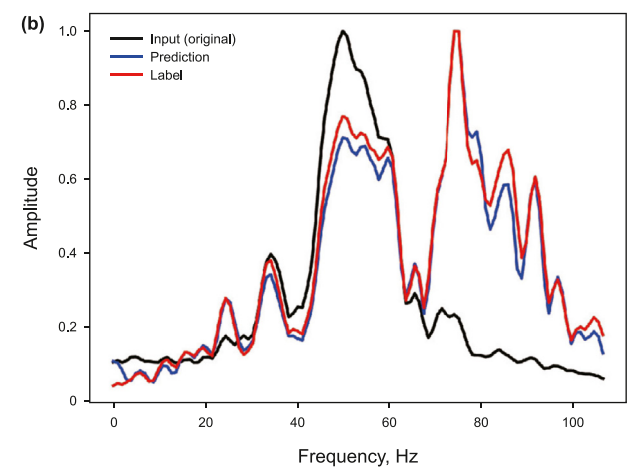


Fig. 11. Amplitude spectra of the network inputs (in black), predictions (in blue), and labels (in red), for the two sample sections in Fig. 10. (a) Spectra of test section-G. (b) Spectra of test section-H.

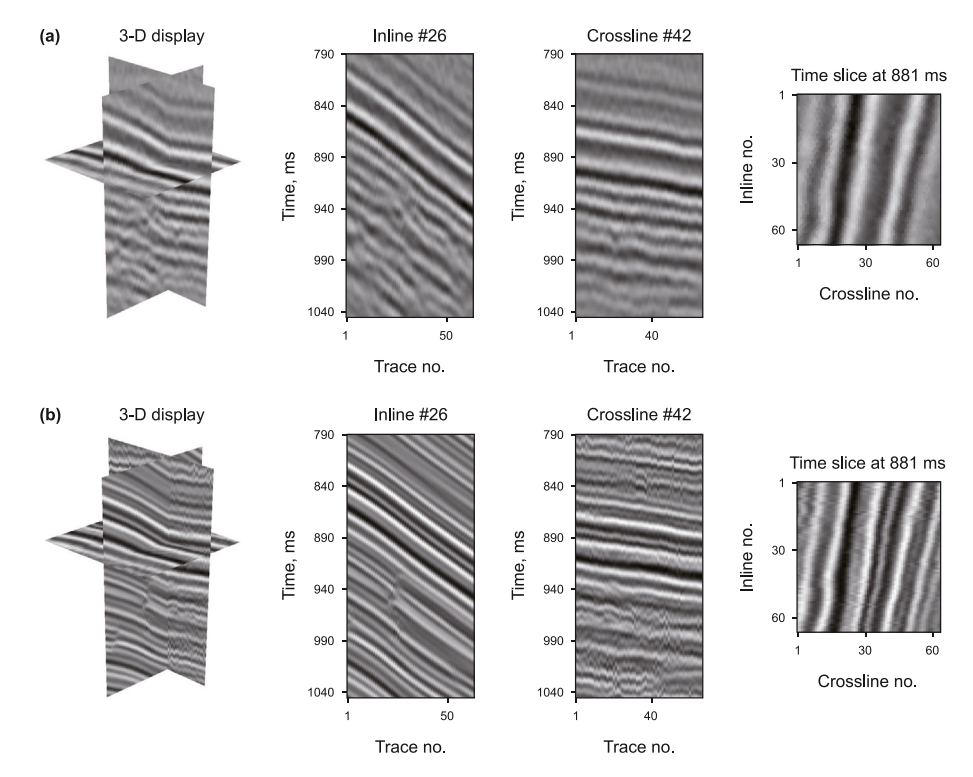
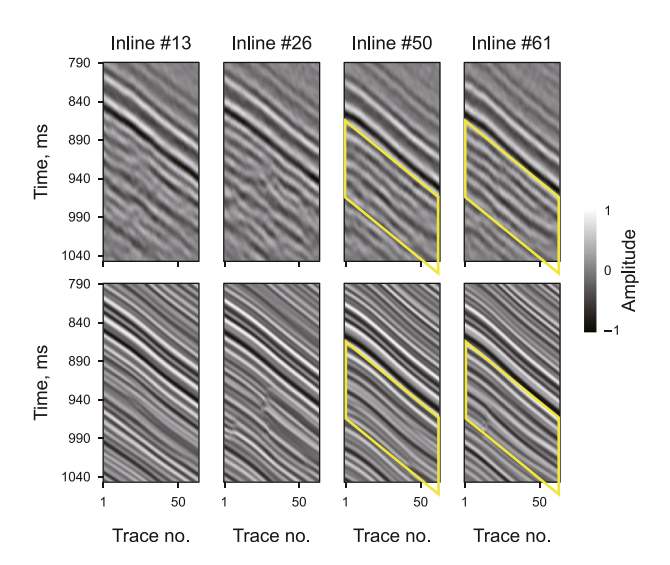
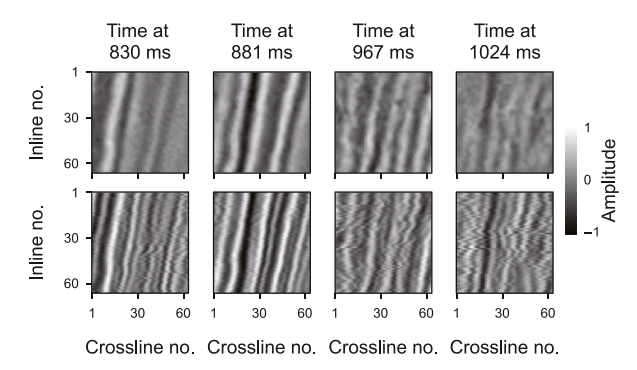


Fig. 12. An overview of the contrast between the field data prior to and after resolution enhancement. (a) Original seismic data. (b) Predicted high resolution data.



**Fig. 13.** SeisResoDiff inference results of the inline sections randomly selected from the field data. The images on the first row display the original field seismic sections, while the second row shows the corresponding predicted high resolution sections.

performance from the figure, where the predictions are highly similar to the labels with little difference. The inference results on test data are presented in Fig. 8. The layout of the images is same as in Fig. 7. The high similarity between the labels and network outputs, as well as the tiny prediction error, can be observed apparently. Moreover, we check the network prediction in the test results from a single seismic trace that is selected randomly from each section (actually from the same location in each section, indicated by red triangles), as shown in the curve plots below seismic images in Fig. 8. We can observe that the predictions are highly consistent with the labels, except the part located in the fault area.



**Fig. 14.** The time slices randomly extracted from the original and predicted field data cube. The images on the first row display the time slices from the original field seismic data, while the second row shows the corresponding time slices in the predicted high resolution data cube.

# 4.2. Resolution enhancement with denoising

In reality, there is more or less noise in post-stack field data, though a few specific seismic denoising steps may have been conducted. Fortunately, denoising is an intrinsic characteristic of diffusion models. Moreover, the data with diverse levels of random noise in addition to noise-free data can be included in the network inputs as the condition of diffusion models. Therefore, we complete experiments on the noisy synthetic data at different noise levels to test if noise can be eliminated while resolution is enhanced.

To make the synthetic data more realistic, we add not only the white noise at different signal-noise ratios (SNR), but also band-limited Gaussian noise with different filtering windows, to the clean data to obtain noisy network inputs. For noise adding in the data preparation, the SNR of the data with white noise float from 2 dB to 18 dB. In addition, when adding the noise to data, the white Gaussian noise is selectively low-pass filtered with an upper cut-off

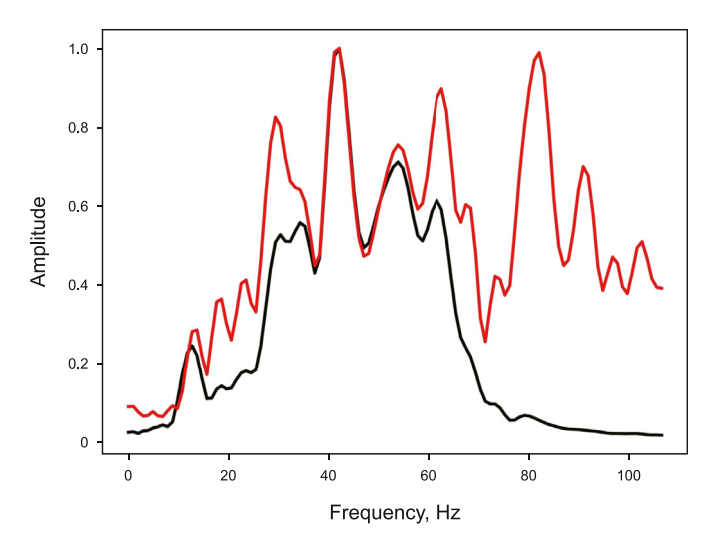


Fig. 15. Amplitude spectra of the original field data (in black) and predicted data (in red).

frequency ranging from 80 Hz to 150 Hz. Each piece of data is assigned randomly to add with the noise or not. There are two reasons for adopting this noise adding strategy: (1) The noise existing in the field data in this research looks like band-limited Gaussian noise mainly; (2) The noise differs a bit across different sections, and it is necessary to extend the diversity of the training dataset. It should be noted that we only add noise to the low resolution input data as opposed to the labels (i.e. high resolution expectations). The training set-up maintains same as that in previous noise-free tests.

Figs. 9 and 10 show some examples of results in training and inference, respectively. We exhibit the examples from the network inputs with different SNR levels, different noise frequency bands, and different subsurface structures. For some cases with relatively complex structures like faults, the diffusion model is able to precisely recover the seismic events split by the faults (Figs. 9(a), 9(b),

and 10(b)). In some cases, even if seismic events are contaminated significantly because of low SNR, the signals can be reconstructed correctly as well (e.g. Figs. 9(a) and 10(b)). Like in Fig. 8, we show curve comparisons from designated seismic traces in this case in Fig. 10 as well. There is some mismatch between the predictions and the labels in this scenario where the diffusion model enhances resolution from noisy data in low resolution. However, the prediction errors mainly occur upon the amplitude mismatch with minor phase shift. Apart from the high similarity and low prediction discrepancy between the outputs and labels in time domain, we can observe the effectiveness of the frequency extension from the spectra in Fig. 11. There is little inconsistency between the spectra of the original and predicted data. The experimental results demonstrate the good performance of the diffusion model. Denoising is an accessional feature of the diffusion-model-based resolution enhancement. We then infer the trained diffusion model to the field case later on.

# 5. Field data example

The field data used in this research are a subset of the data from the previous work (Zhang et al., 2023), with dimensions (inline numbers, crossline numbers, time samples) of (67, 64, 256) and a sampling rate of 1 ms, extracted from a 3-D survey. Similar to the synthetic data example, here, 2-D inline sections within the 3-D low-resolution data cube are input into the trained diffusion model, section by section. Subsequently, the 2-D outputs are assembled to form the 3-D predicted data cube. It is not necessary to fine-tune the diffusion model for field case, because the synthetic training dataset used above is created based on the field data, and the model is trained accordingly. We analyze the resolution enhancement results and show the effectiveness of our approach in terms of the comparisons on both inline sections and time slices. the amplitude spectra prior to and after the enhancement, and the result comparisons with the real well-logging profiles. An overview of the comparison between the original field data and its corresponding resolution enhanced data is given in Fig. 12, from which we can see a great improvement of seismic resolution. Although the

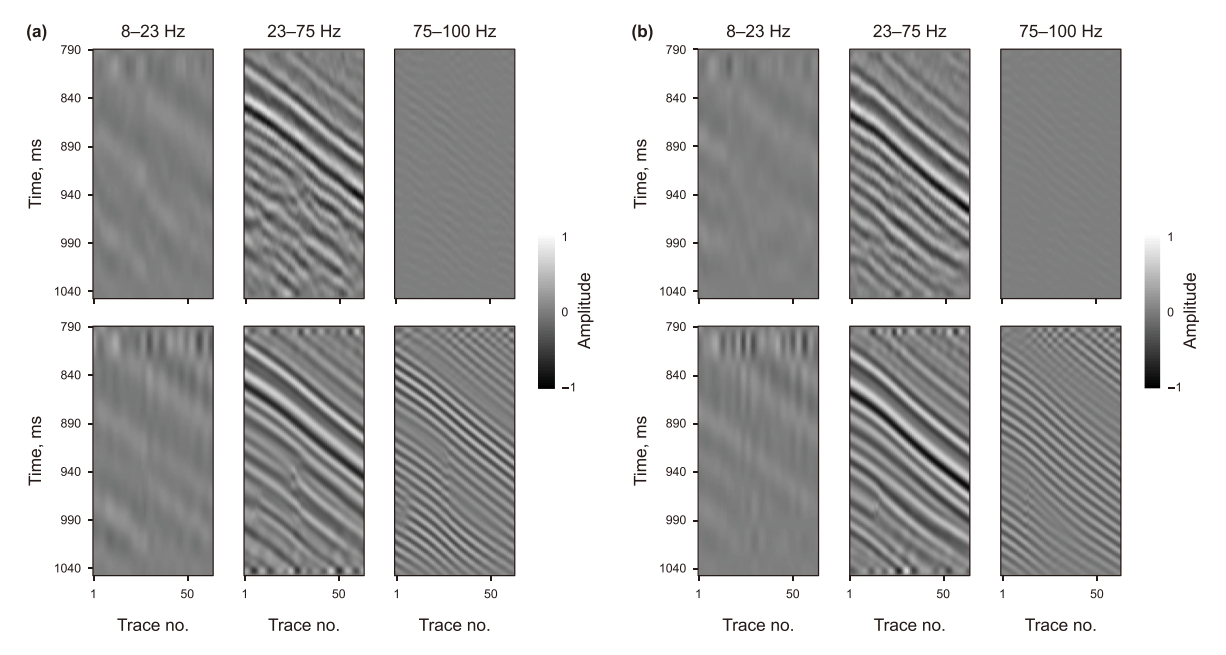


Fig. 16. Seismic sections of the original and corresponding predicted data among different frequency bands. The first row in each subplots displays the inline sections of the original low-resolution data, and the second rows display the inline sections of the predicted high-resolution data. (a) Inline #26. (b) Inline #61.

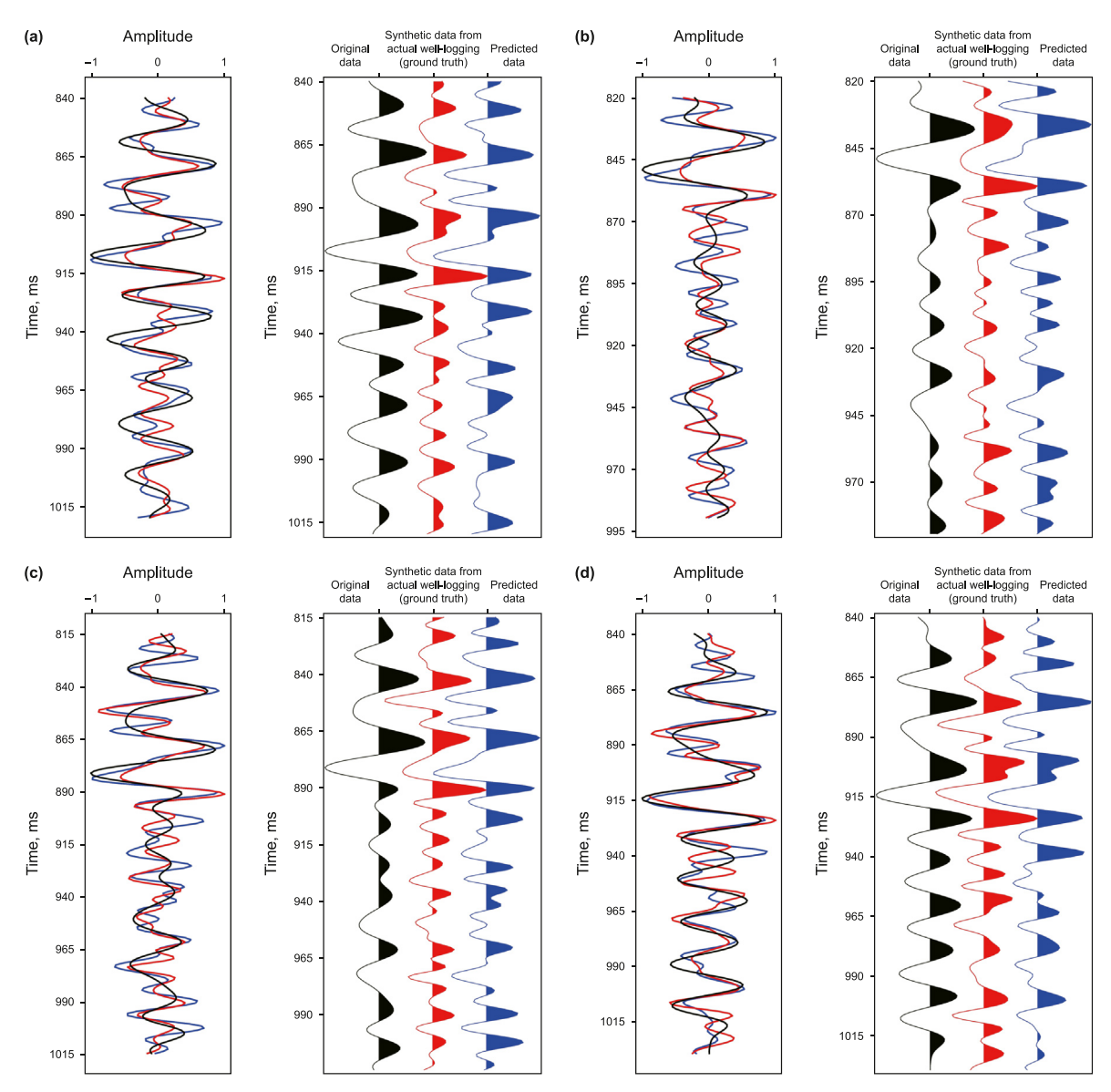


Fig. 17. The data at well locations from the original data (in black), the predicted data (in blue), and the synthetic data using the real impedance from well-logging (in red). The wiggles in the graphs on the left and right in each subplot are displayed in waveform and wiggle plus variable area, respectively. (a) Well #1. (b) Well #3. (c) Well #5. (d) Well #2.

**Table 1**The similarity measurement between the predicted data and the synthetic data using the real well impedance, as well as the original data and the synthetic data using the real well impedance, with different metrics (Correlation coefficient (Corr), R<sup>2</sup>, and Semblance) for each well.

Metric	Well #1 Wel		Well #2		Well #3		Well #4		Well #5		Well #6	
	Predicted	Original	Prediction	n Original	Predicted	Original	Predicted	Original	Predicted	Original	Predicted	Original
Corr R <sup>2</sup> Semblance	0.778 0.600 0.864	0.714 0.504 0.825	0.785 0.586 0.892	<b>0.789</b> <b>0.602</b> 0.892	0.703 0.493 0.834	0.666 0.398 0.830	0.683 0.465 0.815	0.588 0.343 0.769	0.791 0.625 0.881	0.692 0.427 0.845	0.732 0.512 0.862	0.651 0.388 0.819
Metric	Well #7		W	Vell #8		Well #9		Well	#10		Well #11	
	Predicted	l Orig	inal P	redicted	Original	Predicted	Original	Predi	cted O	riginal	Predicted	Original
Corr R <sup>2</sup> Semblance	0.678 0.443 0.831	0.72 0.50 0.85	9 0.	.737 <b>.537</b> .861	0.738 0.535 0.863	0.764 0.582 0.873	0.662 0.437 0.810	0.817 0.662 0.894	0.	772 589 879	0.795 0.627 0.879	0.801 0.637 0.894

diffusion model processes 2-D inline sections in our tests, the crossline sections and time slices extracted from the 3-D predicted

data cube reveal acceptable prediction results. These results exhibit enhanced resolution and good continuity of seismic events.

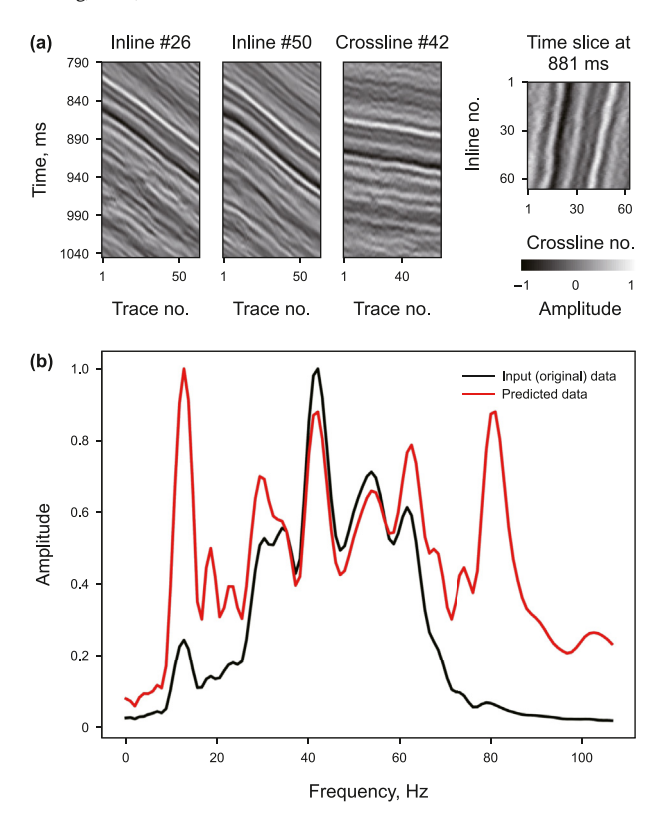


**Fig. 18.** The field high resolution results inferred by the network trained on clean synthetic training data. **(a)** Results displayed in time domain. **(b)** Amplitude spectra of the original (in black) and predicted (in red) data.

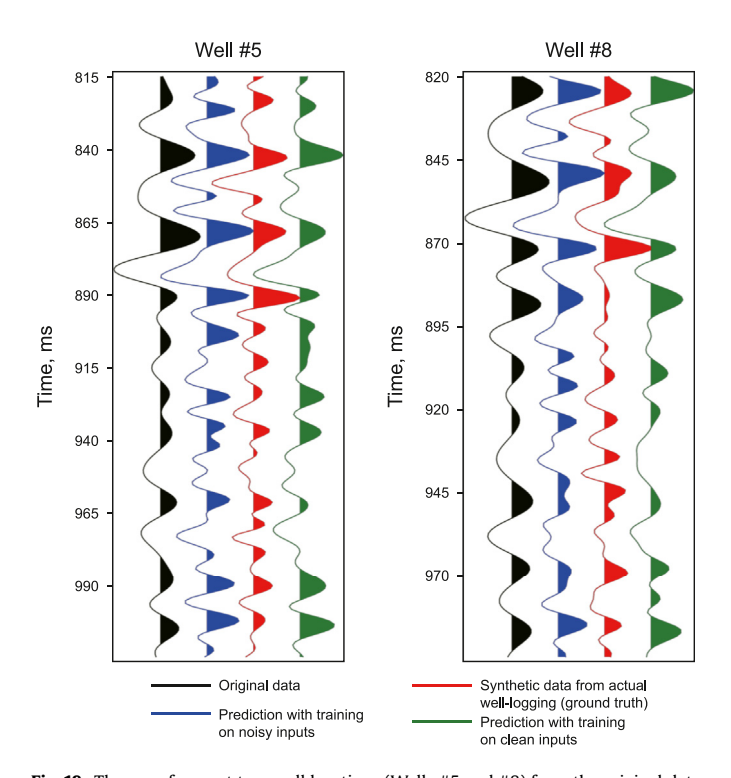


**Fig. 19.** The waveforms at two well locations (Wells #5 and #8) from the original data (in black), the data predicted using the network trained on noisy inputs (in blue), the data predicted using the network trained on clean inputs (in green), and the synthetic data using real impedance from well-logging (in red).

## 5.1. Comparison in the time domain

We randomly select the sections of inlines #13, #26, #50, and #61 as the result examples shown in Fig. 13. It can be observed that the seismic events in the network predictions are highly resolved compared to the original sections. High resolution is not only shown on the increase of seismic events but also the enhancement of geological structures. For example, regarding the section of inlines #50 and #61, there are a few seismic events with similar intensity (amplitude) evenly spaced from time 865–950 ms or so in the original seismic sections, while in the predicted sections, it is easier to identify different strata with amplitude variation and tiny structures like slight folds and small faults (highlighted by yellow parallelograms in Fig. 13). Compared with the previous approach (Zhang et al., 2023) applied to the same field data, the proposed scheme in this work provides cleaner predictions in a new style. For the distribution of some subsurface layers, the results predicted by the diffusion model show more reasonable delineation, compared to the Figs. 4 and 9 in Zhang et al. (2023).

In addition to the inline sections, time slices are extracted to display another side of the resolution enhancement data cube. The slices at 830, 881, 967, and 1024 ms are randomly chosen to be shown in Fig. 14, representing different parts from top to bottom in the data. Although the result data cube is composed by predicted inline sections, the seismic events in time slices show good continuities and the improvement of structural details, implying the robustness and reliability of our proposed scheme.

## 5.2. Analysis in the frequency domain

The amplitude spectra of both the original field data and resolution enhanced data are plotted in black and red curves, respectively, in Fig. 15. The spectra are normalized to the range of [0,1] to give a intuitive comparison. The figure shows frequency extrapolation of the resolution enhanced result in both low and high frequency parts, compared to the spectrum of the original data. The enhancement of low frequencies near 20 Hz displays improvement of stereoscopic effects in seismic sections, and the extrapolation of high frequencies reveals the increase of seismic events. The magnitude of medium frequencies maintains the same or a bit enhanced, implying little signal leakage while enhancing seismic resolution.

To further analyze the results, we split the frequency band into low, medium, and high parts, corresponding to 8-23 Hz, 23-75 Hz, and 75-100 Hz, to check the signals from those frequency components individually. We extract the original and predicted field data from the split frequency bands and display two sample sections in time domain, compared in Fig. 16. Regarding the low frequency components, the predicted data possess clearer low frequency signals apparently. For the medium band, the predicted data show similar characteristics to the original data but with better continuity of seismic events and clearer subsurface structures. In the high frequency band, the resolution enhanced data are obviously superior to the original data in terms of the signal energies and the structures. However, we can also observe the noise enhancement in the predicted data at the top and bottom parts of the sections, especially in the low and high frequency bands. We intend to deal with this issue in the future.

# 5.3. Comparison with actual well-logging

For field seismic data, regardless how detailed analysis we have completed towards the high resolution results in both time and frequency domains, the most convincing evidence is that the resolution enhanced data at the well locations can be consistent with

**Table 2**The similarity measurement between the predicted data and the synthetic data in different metrics (Correlation coefficient (Corr),  $R^2$ , and Semblance) for each well. The predicted data are obtained with training the network on clean inputs, and the synthetic data at well locations are simulated with the real well impedance.

Metric	Well #1	Well #2	Well #3	Well #4	Well #5	Well #6	Well #7	Well #8	Well #9	Well #10	Well #11
Corr	0.675	0.712	0.616	0.616	0.631	0.619	0.677	0.665	0.571	0.717	0.723
$R^2$	0.398	0.586	0.316	0.342	0.318	0.247	0.437	0.385	0.261	0.436	0.486
Semblance	0.824	0.855	0.806	0.802	0.815	0.809	0.832	0.831	0.781	0.859	0.859

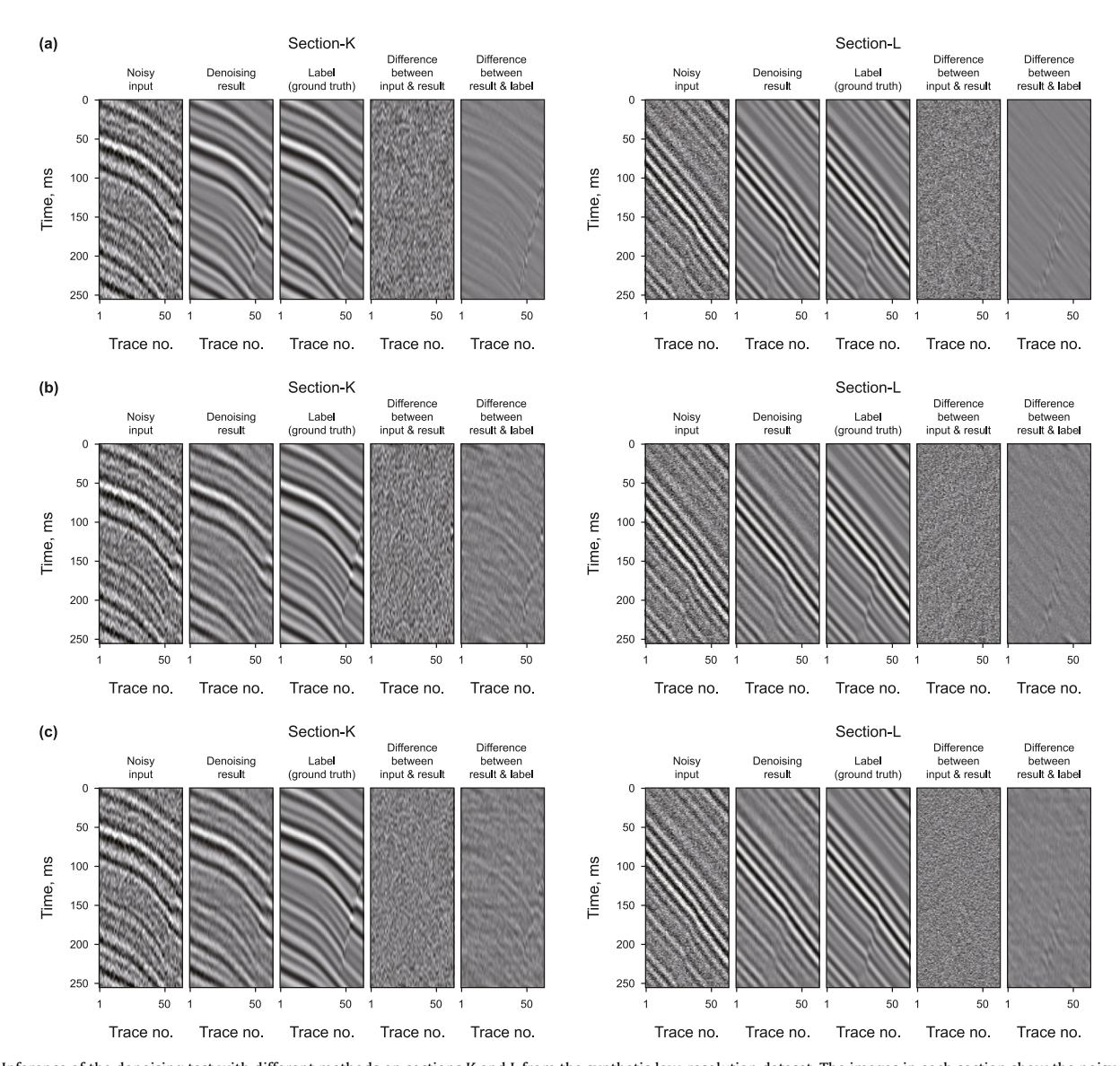


**Fig. 20.** Inference of the denoising test with different methods on sections K and L from the synthetic low-resolution dataset. The images in each section show the noisy input, the denoising result, the label, the difference between the input and the result, and the difference between the result and the label. **(a)** The conditional diffusion model (SeisResoDiff). **(b)** FX-Deconv. **(c)** MSSA.

 Table 3

 Setups of the denoising test, and the SNR values of the test sections after denoising based on FX-Deconv, MSSA, and SeisResoDiff (The numbers in bold denote the higher).

	Section-I	Section-J	Section-K	Section-L
SNR after adding Gaussian white noise, dB	-2	-2	-2	2
Upper cut-off frequency (if low-pass filtering), Hz	/	82	128	1
Ultimate SNR of noisy inputs, dB	-2	5.84	4.15	2
SNR after denoising (FX-Deconv), dB	11.30	10.71	10.11	13.71
SNR after denoising (MSSA), dB	11.35	11.23	10.37	14.44
SNR after denoising (proposed SeisResoDiff), dB	18.67	16.15	15.22	17.94

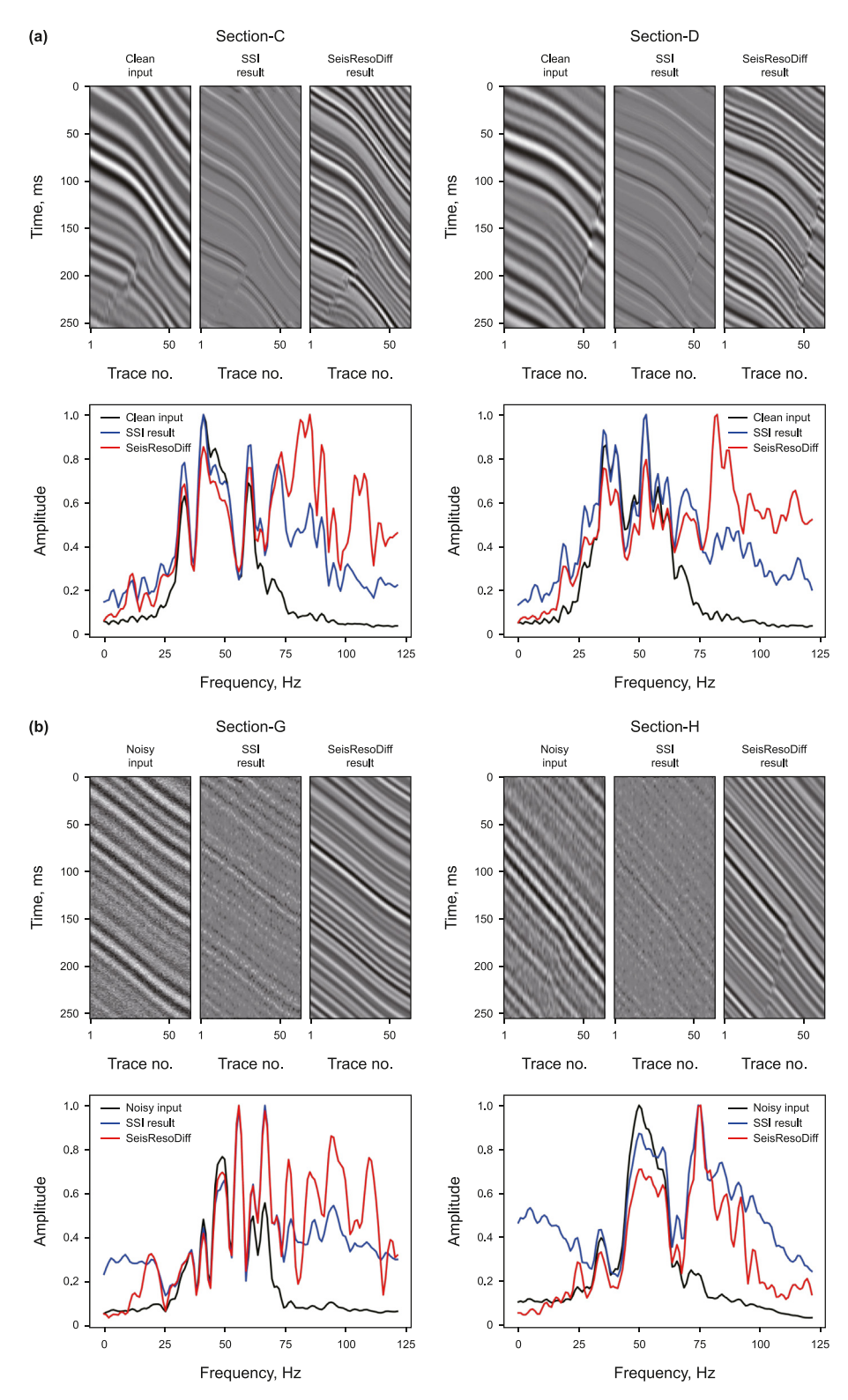


Fig. 21. Sections and spectra of the original data and high-resolution results on clean and noisy synthetic test data. The high-resolution results are obtained using the SSI method and SeisResoDiff. (a) Results using original clean data. (b) Results using original noisy data.

the synthetic data based on the actual well-logging (i.e. a single synthetic trace using well-logging data for each well). As we have mentioned in the data preparation, a total of 11 wells located in this field survey are used for data fitting to generate pseudo-wells. However, there is no participation of the real well-logging

profiles in network training, meaning that all of the well-logging data can be used for validating the accuracy of high resolution predictions. To acquire the synthetic seismic data from the well-logging profiles, first, we calculate the reflectivities based on P-wave velocity and rock density. Then, we take the broad-band

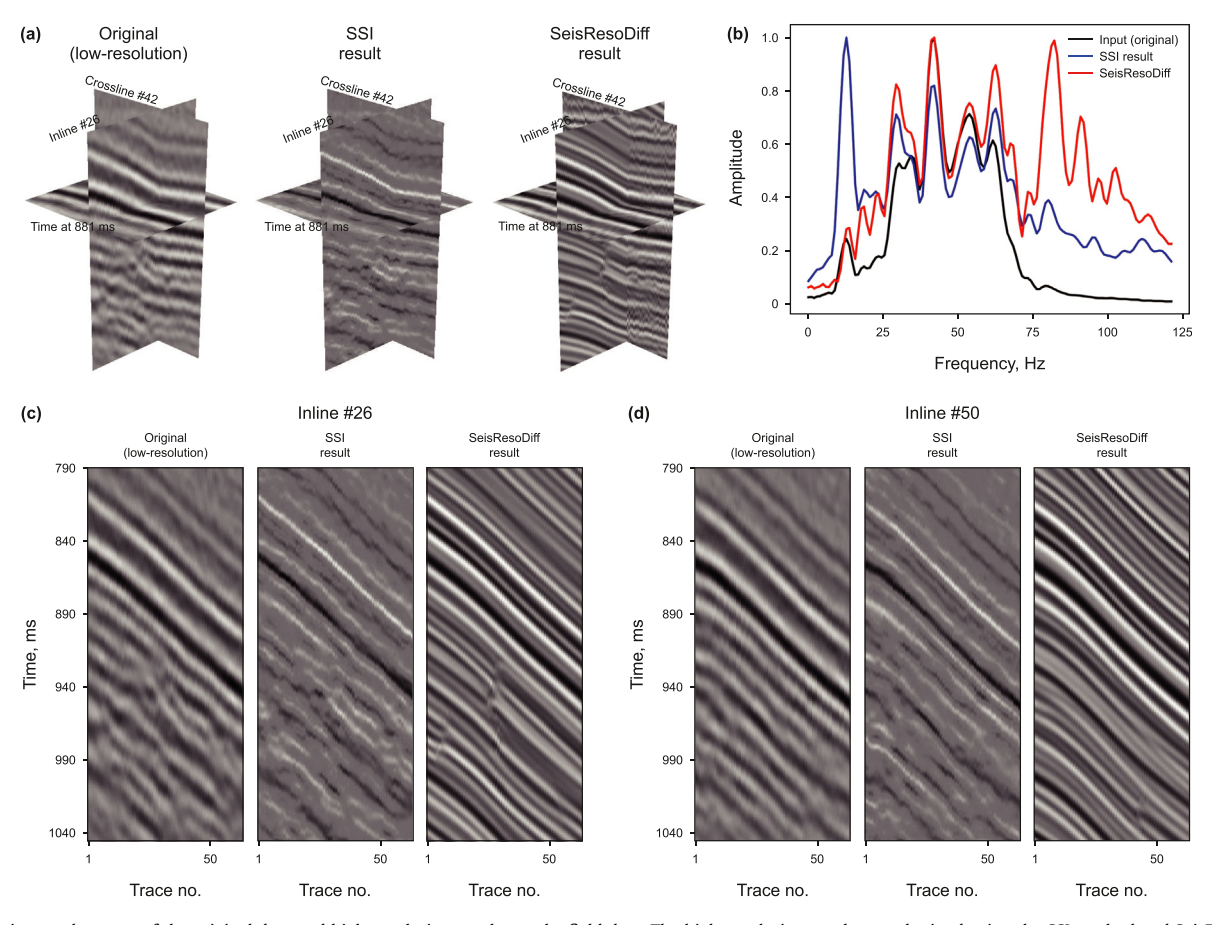


Fig. 22. Sections and spectra of the original data and high-resolution results on the field data. The high-resolution results are obtained using the SSI method and SeisResoDiff. (a) The 3-D display of the original data and high-resolution results. (b) Spectra of the original data and high-resolution results. (c) Sections of the original data and high-resolution results from Inline #26. (d) Sections of the original data and high-resolution results from Inline #50.

**Table 4**The similarity measurement between the high-resolution result by SSI and the synthetic data using different metrics (Correlation coefficient (Corr),  $R^2$ , and Semblance) for each well. The synthetic data at well locations are simulated with real well impedance.

Metric	Well #1	Well #2	Well #3	Well #4	Well #5	Well #6	Well #7	Well #8	Well #9	Well #10	Well #11
Corr	0.578	0.646	0.554	0.533	0.530	0.477	0.552	0.519	0.502	0.650	0.654
R <sup>2</sup>	0.078	-0.270	0.055	0.010	-0.157	-0.565	0.135	-0.185	-0.133	-0.131	0.166
Semblance	0.789	0.800	0.775	0.768	0.762	0.726	0.775	0.756	0.752	0.809	0.823

wavelet that has been used to generate high resolution labels in network training, and let the reflectivities convolve with the wavelet to simulate the seismic data at the well locations. Finally, inspired by the practice of seismic-well tie where people check the alignment of seismic events between the observed seismic data and the synthetic data with well-logging profiles, we compare the wiggle alignment, and measure the similarity with different metrics (Correlation coefficient (Corr),  $R^2$ , and Semblance), between the predicted data and the synthetic data at the well locations, as well as the original data and the synthetic data at the well locations, shown in Fig. 17 and Table 1, respectively.

In Table 1, each number represents the similarity measurement between the field data (predicted or original) and the synthetic data for the corresponding well. The values from all of metrics range from 0 to 1, and the approach to 1.0 of the values means the tendency of consistence between the comparative data. The numbers in bold denote the higher one between the two values for

the specific metric in that well. From the measurement in Table 1, it can be counted that there are 7 wells in which the predicted data show higher values than the original data for all of the 3 metrics, indicating that the predicted data are more consistent with the synthetic data than the original field data for 7 out of 11 wells. Compared with the results in the previous research (Zeng et al., 2023), the resolution enhancement in this work on Well #1 that is the test well in the previous work performs higher correlation (0.778 versus 0.72) with the synthetic data (ground truth). We can observe the difference intuitively from Fig. 17, in which the subplots (a) to (c) show the data for 3 wells randomly chosen from the 7 wells. For the residual 4 wells (Wells #2, #7, #8, #11), although the metric comparisons are not encouraging, the wiggles offer an inspiring comparison. From Fig. 17(d) that displays the wiggles from Well #2, the high resolution prediction shows good alignment with the synthetic data (ground truth) for seismic events whereas the original low resolution data do not.

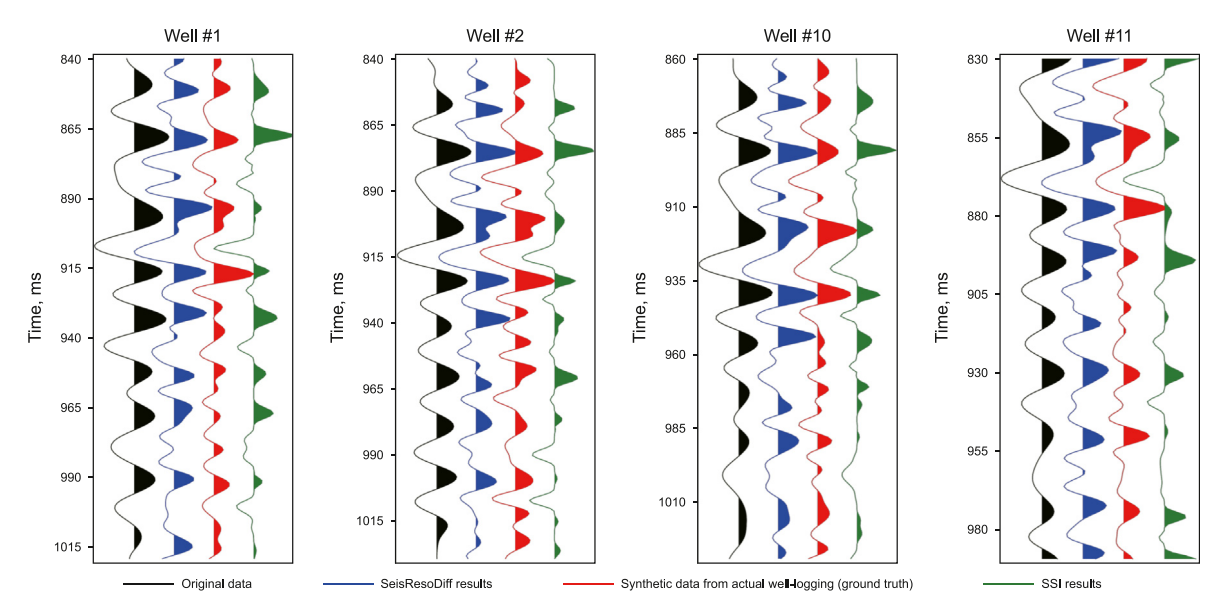


Fig. 23. The waveforms at four well locations (Wells #1, #2, #10, and #11) from the original data (in black), the data predicted by SeisResoDiff (in blue), the high-resolution results by SSI (in green), and the synthetic data using real impedance from well-logging (in red).

## 6. Discussion

# 6.1. Performance of training on clean data

The results from the field data example above are on the basis of the diffusion model trained with noisy synthetic data. However, if we train the model on clean data when other setups remain unchanged, we would obtain totally different results, shown in Figs. 18 and 19. First, from the sections in Fig. 18, we can observe stronger stereoscopic effect which relates to the extrapolation of low frequencies. This effect can be verified in the low frequency part from the spectrum (Fig. 18(b)) as well. Second, the general appearance of the sections looks more natural with many newly generated thin layers - the extrapolation of high frequencies. Nevertheless, most of the extrapolated thin layers are not geologically reasonable. And the correlation coefficients decrease heavily when comparing the values with that in the case where we train the network on noisy inputs (Table 2). We can also observe the less alignment between the predicted and the synthetic data from wells (Fig. 19), indicating the errors of resolution enhancement in this case. Therefore, training with noisy data is more reliable.

# 6.2. Denoising test of the conditional diffusion model

The proposed SeisResoDiff has been validated good performance in resolution enhancement. To further highlight the superiority of the proposed scheme, we test the denoising ability of the conditional diffusion model separately on the original lowresolution seismic data. Using the same framework of the conditional diffusion model as in resolution enhancement, the diffusion model is still conditioned on the noisy low-resolution data and starts the reverse process from pure Gaussian noise, while the desired outputs, as well as the labels, are corresponding clean versions of the low-resolution data rather than high-resolution data. To create the training dataset for the denoising experiment, we add Gaussian noise with SNR ranging from -5 dB to 10 dB and filter the noise on partial seismic sections with upper cut-off frequencies ranging from 75 Hz to 140 Hz. The same set of hyperparameters as in resolution enhancement is adopted during training. The inference results on the test dataset with the trained

diffusion model are displayed in Fig. 20(a). The SNR values computed before and after denoising on the test dataset are exhibited in Table 3. Apart from that, we implement two other conventional methods, f-x deconvolution (FX-Deconv) (Canales, 1984) and multichannel singular spectrum analysis (MSSA) (Oropeza and Sacchi, 2011), for denoising on the same test dataset, and display the results in Fig. 20 and Table 3 as well. From section comparisons of the denoising results in Fig. 20, we can observe that the diffusion model achieves the cleanest denoising image with clear delineation of faults among the results from all three approaches. The SNR comparisons from Table 3 provide quantitative evidence of the diffusion model's superior performance, showing the largest SNR improvement in denoising. Nevertheless, considering that the diffusion model in this study requires labels for training, it does not have an advantage in computational efficiency compared to the conventional methods. Additionally, the network is prone to generalization issues. It is meaningful to conduct specialized and comprehensive investigations of diffusion models' abilities on denoising tasks in our future work.

## 6.3. Comparisons with sparse-spike inversion (SSI)

We use the conventional method SSI, known for its effectiveness and popularity in seismic resolution enhancement, as a benchmark to further evaluate the performance of SeisResoDiff. The SSI method is applied to the same synthetic test dataset and field data used in the SeisResoDiff experiments. The wavelet required for SSI in both synthetic and field data examples is the same one extracted from the field data. Figs. 21 and 22 show the SSI results on synthetic and field data, respectively. The corresponding SeisResoDiff results are also displayed for comparison.

From Fig. 21, we can observe that both SSI and SeisResoDiff significantly improve seismic resolution. However, SeisResoDiff performs much better than SSI when applied to noisy low-resolution data, demonstrating SeisResoDiff's robustness. Observing Figs. 21 and 22, SSI tends to provide data with strong low-frequency energy, whereas SeisResoDiff predicts more high-frequency details. We calculate the similarity measurements of the waveforms at well locations, as shown in Table 4, and select the profiles at four well locations where the similarity measurements

are generally higher in Table 4, as shown in Fig. 23. From Figs. 22 and 23 and Table 4, it is evident that SeisResoDiff comprehensively outperforms SSI on the given field data, particularly in terms of the sections and the waveforms at well locations.

## 6.4. Challenges and future work

The experiments in this research are still initial tests of seismic resolution enhancement applications using diffusion models. Although the training process is not typical of supervised learning, the diffusion model in SeisResoDiff is trained with labels to generate the desired outputs. Therefore, the diffusion model may encounter generalization issues when applied to the data outside the training data distribution. In practice, the data generation scheme used in this research has been validated as an effective way to mitigate the generalization issue, even when there is a distribution gap between the field data used in inference and the synthetic training data. We recommend either creating the corresponding synthetic training data based on the features of target field data, or adopting transfer learning strategies when applying SeisResoDiff to new datasets. Otherwise, it is necessary to study reliable unsupervised methods with diffusion models or other deep learning techniques for resolution enhancement.

Furthermore, there are other interesting tests to be explored in future work. For instance, although we have obtained promising results through current proposed scheme and experimental setups, the results need to be improved extensively. To this end, we consider adding well-logging constrains to the training procedure, and exploring new ways for generating training data. In addition, it is necessary to improve the inference efficiency, as the current application performs every single sampling step during inference to produce the results. Fortunately, there have been accelerated sampling methods proposed recently, and we consider integrating them into our scheme. The purpose of this work is mainly to show the feasibility of diffusion-model-based resolution enhancement.

## 7. Conclusion

In line with the popularity and robust capabilities of generative diffusion models in recent years, we employ a conditional diffusion model based on DDPM for seismic resolution enhancement. The proposed scheme adopts a DDPM conditioned on low-resolution seismic inputs to extrapolate both low- and high-frequency components, thus enhancing resolution. We devise an effective workflow for simulating pseudo well-logging profiles, thereby generating a substantial amount of training data. The experiments conducted using both synthetic and field data examples, yield

competitive results, validating the rationale and effectiveness of our proposed scheme. The results, presented in both the time and frequency domains, along with quantitative comparisons with synthetic data based on real well-logging at the well locations, comprehensively demonstrate the robust performance of SeisResoDiff. By employing a diffusion model conditioned on noisy training inputs, we are not only able to obtain broad-band signals but also effectively eliminate noise present in the original low-resolution data. Compared to the conventional method SSI, Seis-ResoDiff shows superior high-resolution results in the time domain sections and in prediction consistency with well-logging. Our application serves as an initial reference and showcases the significant potential of diffusion-model-based seismic resolution enhancement.

## **CRediT** authorship contribution statement

**Hao-Ran Zhang:** Writing — review & editing, Writing — original draft, Visualization, Validation, Supervision, Software, Resources, Project administration, Methodology, Investigation, Formal analysis, Data curation. **Yang Liu:** Writing — review & editing, Supervision, Project administration, Funding acquisition, Conceptualization. **Yu-Hang Sun:** Writing — review & editing, Software, Resources, Methodology, Data curation. **Gui Chen:** Writing — review & editing, Software, Conceptualization.

## Acknowledgments

This work was supported by the National Natural Science Foundation of China (NSFC): Grant number 42274147. We thank Ricard Durall from the Fraunhofer Institute for Industrial Mathematics (Fraunhofer ITWM) in Germany for sharing his expertise on diffusion models. We are also grateful to Yang Gao and our colleague Jiangtao Ma from China University of Petroleum (Beijing) for their valuable discussions. Additionally, we thank the BGP Research and Development Center for generously providing the field data.

# Appendix A. Derivation of the DDPM optimization objective

As illustrated in section 2.3, the reverse process of DDPM is formed into an optimization problem, in which we seek to minimize the distance between the learnable distribution  $p_{\theta}$  (relying on network weights  $\theta$ ) and the reverse of the diffusion process q. Using Kullback-Leibler (KL) divergence (Kullback and Leibler,  $1951D_{\text{KL}}(q \parallel p_{\theta})$  for the distance measurement between the two distributions  $p_{\theta}$  and q, the objective function can be formulated as

$$\begin{aligned} \underset{\theta}{\operatorname{argmin}} D_{\mathrm{KL}}(q \parallel p_{\theta}) &= \underset{\theta}{\operatorname{argmin}} \sum_{i=1}^{m} q(x_{i}) \log \left( \frac{q(x_{i})}{p_{\theta}(x_{i})} \right) \\ &= \underset{\theta}{\operatorname{argmin}} \left( \sum_{i=1}^{m} q(x_{i}) \log q(x_{i}) - \sum_{i=1}^{m} q(x_{i}) \log p_{\theta}(x_{i}) \right) \\ &= \underset{\theta}{\operatorname{argmin}} \left( - \sum_{i=1}^{m} q(x_{i}) \log p_{\theta}(x_{i}) \right) (q \text{ is known}) \\ &= \underset{\theta}{\operatorname{argmin}} \mathbb{E}_{x \sim q(x)} [-\log p_{\theta}(x)] \text{ (Definition of expectation } \mathbb{E}) \end{aligned}$$

where the function "argmin" stands for "argument of the minimum" and herein outputs a set of network weights  $\theta$  that minimize  $D_{\mathrm{KL}}(q\|p_{\theta})$  over the domain of network weights, and q represents the diffusion which is already designated and nothing related to the network. The derivation above reveals that the network optimization pursues a largest  $p_{\theta}$ . In particular, we need to obtain the largest probability for reconstructing the original seismic data  $\mathbf{x}_0$ .

Now the optimization problem can be transformed into the maximization of variational lower bound ( $L_{VLB}$ ) for the log-likelihood (i.e.  $logp_{\theta}(\mathbf{x}_0)$ ) by the derivation below:

and the standard Gaussian prior, and this term has no trainable weights so it is a constant. The term  $L_0$  is the reconstruction term which reflects the last step of the reverse process and is actually dominated by the denoising matching term  $L_{\tau}$ . The term  $L_{\tau}$  measures the matching between the predicted reverse process  $p_{\theta}(\mathbf{x}_{t-1}|\mathbf{x}_t)$  and the real reverse process  $q(\mathbf{x}_{t-1}|\mathbf{x}_t,\mathbf{x}_0)$ . Then, the term  $L_{\tau}$  becomes the optimization objective.

By Bayes rule, the denoising process  $q(\mathbf{x}_{t-1}|\mathbf{x}_t,\mathbf{x}_0)$  can be formed into

$$\begin{split} \log p_{\theta}(\boldsymbol{x}_0) &= log \ p_{\theta}(\boldsymbol{x}_0) \int q(\boldsymbol{x}_{1:T}|\boldsymbol{x}_0) d\boldsymbol{x}_{0:T} &= \int q(\boldsymbol{x}_{1:T}|\boldsymbol{x}_0) log \ p_{\theta}(\boldsymbol{x}_0) d\boldsymbol{x}_{0:T} \\ &= \mathbb{E}_{q(\boldsymbol{x}_{1:T}|\boldsymbol{x}_0)} [log \ p_{\theta}(\boldsymbol{x}_0)] \\ &= \mathbb{E}_{q(\boldsymbol{x}_{1:T}|\boldsymbol{x}_0)} \left[ log \left( \frac{p_{\theta}(\boldsymbol{x}_{0:T})}{p_{\theta}(\boldsymbol{x}_{1:T}|\boldsymbol{x}_0)} \frac{q(\boldsymbol{x}_{1:T}|\boldsymbol{x}_0)}{q(\boldsymbol{x}_{1:T}|\boldsymbol{x}_0)} \right) \right] \\ &= \mathbb{E}_{q(\boldsymbol{x}_{1:T}|\boldsymbol{x}_0)} \left[ log \left( \frac{p_{\theta}(\boldsymbol{x}_{0:T})}{q(\boldsymbol{x}_{1:T}|\boldsymbol{x}_0)} \right) \right] - \mathbb{E}_{q(\boldsymbol{x}_{1:T}|\boldsymbol{x}_0)} \left[ log \left( \frac{p_{\theta}(\boldsymbol{x}_{1:T}|\boldsymbol{x}_0)}{q(\boldsymbol{x}_{1:T}|\boldsymbol{x}_0)} \right) \right] \\ &= \mathbb{E}_{q(\boldsymbol{x}_{1:T}|\boldsymbol{x}_0)} \left[ log \left( \frac{p_{\theta}(\boldsymbol{x}_{0:T})}{q(\boldsymbol{x}_{1:T}|\boldsymbol{x}_0)} \right) \right] + D_{KL}(q(\boldsymbol{x}_{1:T}|\boldsymbol{x}_0) \parallel p_{\theta}(\boldsymbol{x}_{1:T}|\boldsymbol{x}_0)) \\ &\geq \mathbb{E}_{q(\boldsymbol{x}_{1:T}|\boldsymbol{x}_0)} \left[ log \left( \frac{p_{\theta}(\boldsymbol{x}_{0:T})}{q(\boldsymbol{x}_{1:T}|\boldsymbol{x}_0)} \right) \right] =: L_{VLB} \ (\text{Non-negativity of KL divergence}) \end{split}$$

Furthermore, with Bayes rule as well as some algebraic manipulation (Luo, 2022) and by applying the definition of KL divergence, the  $L_{VLB}$  can be decomposed into KL divergence forms below:

$$\begin{split} L_{\text{VLB}} &= \mathbb{E}_{q(\mathbf{x}_{1:T}|\mathbf{x}_0)} \bigg[ log \bigg( \frac{p_{\theta}(\mathbf{x}_{0:T})}{q(\mathbf{x}_{1:T}|\mathbf{x}_0)} \bigg) \bigg] = L_T + L_\tau + L_0 \\ L_T &= -\mathbb{E}_{q(\mathbf{x}_1|\mathbf{x}_0)} [D_{\text{KL}}(q(\mathbf{x}_T|\mathbf{x}_0) \parallel p_{\theta}(\mathbf{x}_T))] \\ L_\tau &= -\sum_{t=2}^T \mathbb{E}_{q(\mathbf{x}_t|\mathbf{x}_0)} [D_{\text{KL}}(q(\mathbf{x}_{t-1}|\mathbf{x}_t,\mathbf{x}_0) \parallel p_{\theta}(\mathbf{x}_{t-1}|\mathbf{x}_t))] \\ L_0 &= \mathbb{E}_{q(\mathbf{x}_1|\mathbf{x}_0)} [log \ p_{\theta}(\mathbf{x}_0|\mathbf{x}_1)] \end{split} \tag{A.3}$$

where  $L_T$  measures the difference between the noisy network input

$$q(\mathbf{x}_{t-1}|\mathbf{x}_t,\mathbf{x}_0) = \frac{q(\mathbf{x}_t|\mathbf{x}_{t-1},\mathbf{x}_0)q(\mathbf{x}_{t-1}|\mathbf{x}_0)}{q(\mathbf{x}_t|\mathbf{x}_0)}$$
(A.4)

where we have known the exact form of each term on the right side based on the Eqs. (2)–(5) from the main text in the diffusion process:

$$\begin{array}{ll} q(\mathbf{x}_{t}|\mathbf{x}_{t-1},\mathbf{x}_{0}) = q(\mathbf{x}_{t}|\mathbf{x}_{t-1}) &= \mathcal{N}(\mathbf{x}_{t};\sqrt{\alpha_{t}}\,\mathbf{x}_{t-1},\beta_{t}\mathbf{I}) \\ q(\mathbf{x}_{t-1}|\mathbf{x}_{0}) &= \mathcal{N}(\mathbf{x}_{t-1};\sqrt{\overline{\alpha}_{t-1}}\,\mathbf{x}_{0},(1-\overline{\alpha}_{t-1})\mathbf{I}) \\ q(\mathbf{x}_{t-1}|\mathbf{x}_{0}) &= \mathcal{N}(\mathbf{x}_{t};\sqrt{\overline{\alpha}_{t}}\,\mathbf{x}_{0},(1-\overline{\alpha}_{t})\mathbf{I}) \end{array}$$

$$(A.5)$$

Eq. (A.4) can be further derived through Bayes rule expansion as

where we know that the reverse process  $q(\mathbf{x}_{t-1}|\mathbf{x}_t,\mathbf{x}_0)$  at each step t

$$q(\mathbf{x}_{t-1}|\mathbf{x}_{t},\mathbf{x}_{0}) = \frac{\mathscr{N}(\mathbf{x}_{t};\sqrt{\alpha_{t}}\,\mathbf{x}_{t-1},\beta_{t}\mathbf{I})\mathscr{N}(\mathbf{x}_{t-1};\sqrt{\alpha_{t-1}}\,\mathbf{x}_{0},(1-\overline{\alpha}_{t-1})\mathbf{I})}{\mathscr{N}(\mathbf{x}_{t};\sqrt{\overline{\alpha_{t}}}\,\mathbf{x}_{0},(1-\overline{\alpha}_{t})\mathbf{I})}$$

$$\propto \exp\left\{-\frac{\left[\frac{(\mathbf{x}_{t}-\sqrt{\alpha_{t}}\,\mathbf{x}_{t-1})^{2}}{2\beta_{t}}+\frac{(\mathbf{x}_{t-1}-\sqrt{\overline{\alpha}_{t-1}}\,\mathbf{x}_{0})^{2}}{2(1-\overline{\alpha}_{t-1})}-\frac{(\mathbf{x}_{t}-\sqrt{\alpha_{t}}\,\mathbf{x}_{0})^{2}}{2(1-\overline{\alpha}_{t})}\right]\right\}$$

$$\propto \exp\left\{-\frac{1}{2}\left[-\frac{2\sqrt{\alpha_{t}}\mathbf{x}_{t}\mathbf{x}_{t-1}}{1-\alpha_{t}}+\frac{\alpha_{t}\mathbf{x}_{t-1}^{2}}{1-\alpha_{t}}+\frac{\mathbf{x}_{t-1}^{2}}{1-\overline{\alpha}_{t-1}}-\frac{2\sqrt{\overline{\alpha}_{t-1}}\mathbf{x}_{t-1}\mathbf{x}_{0}}{1-\overline{\alpha}_{t-1}}\right]\right\}$$

$$= \exp\left\{-\frac{1}{2}\left(\frac{1}{(1-\alpha_{t})(1-\overline{\alpha}_{t-1})}\right)\left[\mathbf{x}_{t-1}^{2}-2\frac{\sqrt{\alpha_{t}}(1-\overline{\alpha}_{t-1})\mathbf{x}_{t}+\sqrt{\overline{\alpha}_{t-1}}(1-\alpha_{t})\mathbf{x}_{0}}{1-\overline{\alpha}_{t}}\mathbf{x}_{t-1}}\right]\right\}$$

$$\sim \mathscr{N}\left(\mathbf{x}_{t-1};\frac{\sqrt{\alpha_{t}}(1-\overline{\alpha}_{t-1})\mathbf{x}_{t}+\sqrt{\overline{\alpha}_{t-1}}(1-\alpha_{t})\mathbf{x}_{0}}{1-\overline{\alpha}_{t}},\frac{(1-\alpha_{t})(1-\overline{\alpha}_{t-1})}{1-\overline{\alpha}_{t}}\mathbf{I}\right)$$

$$= \mathscr{N}\left(\mathbf{x}_{t-1};\tilde{\mu}(\mathbf{x}_{t},\mathbf{x}_{0}),\tilde{\sigma}^{2}\mathbf{I}\right)$$

satisfies a normal distribution with the mean  $\tilde{\mu}(\mathbf{x}_t, \mathbf{x}_0)$  and variance  $\tilde{\sigma}^2 \mathbf{I}$ .

As we have known from Eq. (6) in the main text, the predicted reverse process  $p_{\theta}(\mathbf{x}_{t-1}|\mathbf{x}_t)$  can be built in a normal distribution with the mean  $\mu_{\theta}(\mathbf{x}_t,t)$  and variance  $\sigma_{\theta}(\mathbf{x}_t,t)$ . Note that the variance  $\tilde{\sigma}^2$  of  $q(\mathbf{x}_{t-1}|\mathbf{x}_t,\mathbf{x}_0)$  is only the function of  $\alpha_t$  that is designated in advance during the diffusion process in our implementation. The reverse process adopts  $\tilde{\sigma}^2$  as the variance as well. Therefore, we have  $p_{\theta}(\mathbf{x}_{t-1}|\mathbf{x}_t) = \mathcal{N}\left(\mathbf{x}_{t-1}; \mu_{\theta}(\mathbf{x}_t,t), \tilde{\sigma}^2\mathbf{I}\right)$ . According to the KL divergence, the optimization objective can be written and derived

$$\mathbf{x}_0 = \frac{\mathbf{x}_t - \sqrt{1 - \overline{\alpha}_t} \epsilon_0}{\sqrt{\overline{\alpha}_t}}, \epsilon_0 \sim \mathcal{N}(\mathbf{0}, \mathbf{I})$$
(A.8)

so that  $\tilde{\mu}$  can only condition on  $\mathbf{x}_t$ :

$$\tilde{\mu} = \frac{\sqrt{\alpha_{t}}(1 - \overline{\alpha}_{t-1})\mathbf{x}_{t} + \sqrt{\overline{\alpha}_{t-1}}(1 - \alpha_{t})\mathbf{x}_{0}}{1 - \overline{\alpha}_{t}} 
= \frac{1}{\sqrt{\alpha_{t}}} \left(\mathbf{x}_{t} - \frac{1 - \alpha_{t}}{\sqrt{1 - \overline{\alpha}_{t}}} \epsilon_{0}\right), \epsilon_{0} \sim \mathcal{N}(\mathbf{0}, \mathbf{I})$$
(A.9)

Since both  $\mu_{\theta}$  and  $\tilde{\mu}$  merely condition on  $\mathbf{x}_{\mathrm{f}}$ , the mean of the predicted reverse process can be set as

$$\begin{aligned} \underset{\theta}{\operatorname{argmin}} L_{\tau} &= \underset{\theta}{\operatorname{argmin}} D_{\operatorname{KL}}(q(\mathbf{x}_{t-1}|\mathbf{x}_{t},\mathbf{x}_{0}) \parallel p_{\theta}(\mathbf{x}_{t-1}|\mathbf{x}_{t})) \\ &= \underset{\theta}{\operatorname{argmin}} D_{\operatorname{KL}}\left( \mathscr{N}\left(\mathbf{x}_{t-1}; \tilde{\mu}(\mathbf{x}_{t},\mathbf{x}_{0}), \tilde{\sigma}^{2}\mathbf{I}\right) \parallel \mathscr{N}\left(\mathbf{x}_{t-1}; \mu_{\theta}(\mathbf{x}_{t},t), \tilde{\sigma}^{2}\mathbf{I}\right) \right) \\ &= \underset{\theta}{\operatorname{argmin}} \frac{1}{2\tilde{\sigma}^{2}} \|\mu_{\theta}(\mathbf{x}_{t},t) - \tilde{\mu}(\mathbf{x}_{t},\mathbf{x}_{0})\|_{2}^{2} \end{aligned} \tag{A.7}$$

where we can know that  $\mu_{\theta}$  is optimized to match  $\tilde{\mu}$ . There is still an issue left: the original seismic data  $\mathbf{x}_0$  in the reverse process are unknown. Nevertheless, from Eq. (5) in the main text, we get

$$\mu_{\theta}(\mathbf{x}_{t},t) = \frac{1}{\sqrt{\alpha_{t}}} \left( \mathbf{x}_{t} - \frac{1 - \alpha_{t}}{\sqrt{1 - \overline{\alpha_{t}}}} \widehat{\epsilon}_{\theta}(\mathbf{x}_{t},t) \right)$$
(A.10)

where  $\hat{\epsilon}_{\theta}(\mathbf{x}_t,t)$  is parameterized by the network that seeks to predict the source Gaussian noise  $\epsilon_0 \sim \mathcal{N}(\epsilon;\mathbf{0},\mathbf{I})$  that determines data  $\mathbf{x}_t$  from  $\mathbf{x}_0$ . Now the optimization problem can be formed into

$$\underset{\theta}{\operatorname{argmin}} D_{\mathrm{KL}}(q(\mathbf{x}_{t-1}|\mathbf{x}_{t},\mathbf{x}_{0}) \parallel p_{\theta}(\mathbf{x}_{t-1}|\mathbf{x}_{t})) = \underset{\theta}{\operatorname{argmin}} \frac{1}{2\tilde{\sigma}^{2}} \|\mu_{\theta}(\mathbf{x}_{t},t) - \tilde{\mu}(\mathbf{x}_{t},\mathbf{x}_{0})\|_{2}^{2}$$

$$= \underset{\theta}{\operatorname{argmin}} \frac{1}{2\tilde{\sigma}^{2}} \frac{(1-\alpha_{t})^{2}}{\alpha_{t}(1-\overline{\alpha}_{t})} \|\widehat{\boldsymbol{\epsilon}}_{\theta}(\mathbf{x}_{t},t) - \boldsymbol{\epsilon}_{0}\|_{2}^{2}$$
(A.11)

from which we obtain the ultimate optimization objective-minimizing the difference between the network output  $\hat{\epsilon}_{\theta}$  and Gaussian noise  $\epsilon_0$ .

## References

- Alali, A., Alkhalifah, T., 2023. Integrating U-Nets into a multiscale full-waveform inversion for salt body building. IEEE Trans. Geosci. Rem. Sens. 61, 1-11. https://doi.org/10.1109/TGRS.2023.3310886.
- Arjovsky, M., Bottou, L., 2017. Towards principled methods for training generative International Conference adversarial networks. In: Representations.
- Berkhout, A.J., 1977. Least-squares inverse filtering and wavelet deconvolution. Geophysics 42, 1369-1383. https://doi.org/10.1190/1.1440798.
- Birnie, C., Alkhalifah, T., 2022. Transfer learning for self-supervised, blind-spot Front. Earth Sci. 10. https://doi.org/10.3389/ denoising.
- Brocher, T.M., 2005. Empirical relations between elastic wavespeeds and density in the Earth's crust. Bull. Seismol. Soc. Am. 95, 2081-2092. https://doi.org/ 10.1785/0120050077
- Canales, L.L., 1984. Random Noise Reduction, vol. 1984. SEG Technical Program Expanded Abstracts, pp. 525-527. https://doi.org/10.1190/1.1894168.
- Cao, S., Sun, Y., Chen, S., 2023. Challenges and solutions to high-resolution data processing for seismic exploration. Coal Geol. Explor. 51, 277-288. https:// doi.org/10.12363/issn.1001-1986.22.11.0841 (in Chinese).
- Cao, S., Yuan, D., 2016. A review of high resolution seismic data processing ap-Xinjiang Pet. Geol. 37, 112–119. https://doi.org/10.7657/ XJPG20160122 (in Chinese).
- Chai, X., Wang, S., Yuan, S., Zhao, J., Sun, L., Wei, X., 2014. Sparse reflectivity inversion for nonstationary seismic data. Geophysics 79, V93–V105. https:// doi.org/10.1190/geo2013-0313.1.
- Chen, G., Liu, Y., 2024. Combining unsupervised deep learning and Monte Carlo dropout for seismic data reconstruction and its uncertainty quantification. Geophysics 89, WA53-WA65. https://doi.org/10.1190/geo2022-0632.1.
- Chen, G., Liu, Y., Zhang, M., Zhang, H., 2022a. Dropout-based robust self-supervised deep learning for seismic data denoising. Geosci. Rem. Sens. Lett. IEEE 19, 1-5. https://doi.org/10.1109/LGRS.2022.3167999.
- Chen, H., Gao, J., Gao, Z., Chen, D., Yang, T., 2021a. A sequential iterative deep learning seismic blind high-resolution inversion, IEEE J. Sel. Top. Appl. Earth Obs. Rem. Sens. 14, 7817–7829. https://doi.org/10.1109/JSTARS.2021.3100502.
- Chen, H., Gao, J., Jiang, X., Gao, Z., Zhang, W., 2021b. Optimization-inspired deep learning high-resolution inversion for seismic data. Geophysics 86, R265–R276. https://doi.org/10.1190/geo2020-0034.1.
- Chen, H., Gao, J., Liu, N., Yang, Y., 2019. Multitrace semiblind nonstationary deconvolution. Geosci. Rem. Sens. Lett. IEEE 16, 1195–1199. https://doi.org/ 10.1109/LGRS.2019.2893924
- Chen, H., Sacchi, M.D., Lari, H.H., Gao, J., Jiang, X., 2023. Nonstationary seismic reflectivity inversion based on prior-engaged semisupervised deep learning method. Geophysics 88, WA115-WA128. https://doi.org/10.1190/geo2022-
- Chen, N., Zhang, Y., Zen, H., Weiss, R.J., Norouzi, M., Chan, W., 2021c. WaveGrad: estimating gradients for waveform generation. In: International Conference on Learning Representations.
- Chen, S., Cao, S., Sun, Y., 2022b. Enhancing the resolution of seismic data based on the non-local similarity. Geophys. Prospect. 70, 1116-1128. https://doi.org/ 10.1111/1365-2478.13202.
- Chen, S., Cao, S., Sun, Y., Lin, Y., Gao, J., 2022c. Seismic time-frequency analysis via time-varying filtering based empirical mode decomposition method. J. Appl. Geophys. 204, 104731. https://doi.org/10.1016/j.jappgeo.2022.104731.
- Cheng, S., Alkhalifah, T., 2023. Robust data driven discovery of a seismic wave
- equation. Geophys. J. Int. 236, 537–546. https://doi.org/10.1093/gji/ggad446. Choi, Y., Jo, Y., Seol, S.J., Byun, J., Kim, Y., 2021. Deep learning spectral enhancement considering features of seismic field data. Geophysics 86, V389-V408. https:// doi.org/10.1190/geo2020-0017.1
- Deng, F., Wang, S., Wang, X., Fang, P., 2024. Seismic data reconstruction based on conditional constraint diffusion model. IEEE Geoscience and Remote Sensing Letters 21, 7502305. https://doi.org/10.1109/LGRS.2024.3371675.
- Dhariwal, P., Nichol, A., 2021. Diffusion models beat GANs on image synthesis. In: Ranzato, M., Beygelzimer, A., Dauphin, Y., Liang, P., Vaughan, J.W. (Eds.), Advances in Neural Information Processing Systems. Curran Associates, Inc.,

pp. 8780-8794

- Dragomiretskiy, K., Zosso, D., 2014. Variational mode decomposition. IEEE Trans. Signal Process. 62, 531-544. https://doi.org/10.1109/TSP.2013.2288675
- Durall, R., Ghanim, A., Fernandez, M.R., Ettrich, N., Keuper, J., 2023. Deep diffusion models for seismic processing. Comput. Geosci. 177, 105377. https://doi.org/ 10.1016/j.cageo.2023.105377.
- Feller, W., 1949. On the theory of stochastic processes, with particular reference to applications. In: Neyman, J. (Ed.), Proceedings of the First Berkeley Symposium on Mathematical Statistics and Probability. University of California Press, Statistical Laboratory of the University of California, Berkeley, Calif, pp. 403-432.
- Gao, J.H., Wang, L.L., Zhao, W., 2009. Enhancing resolution of seismic traces based on the changing wavelet model of seismograms. Chin. J. Geophys. 52, 1289-1300. https://doi.org/10.3969/j.issn.0001-5733.2009.05.018 (in Chinese).
- Gao, Y., Zhang, J., Li, H., Li, G., 2022a. Incorporating structural constraint into the machine learning high-resolution seismic reconstruction. IEEE Trans. Geosci.
- Rem. Sens. 60, 1–12. https://doi.org/10.1109/TGRS.2022.3157064. Gao, Y., Zhao, D., Li, T., Li, G., Guo, S., 2023. Deep learning vertical resolution enhancement considering features of seismic data. IEEE Trans. Geosci. Rem. Sens. 61, 1-13. https://doi.org/10.1109/TGRS.2023.3234617.
- Gao, Z., Hu, S., Li, C., Chen, H., Jiang, X., Pan, Z., Gao, J., Xu, Z., 2022b. A deeplearning-based generalized convolutional model for seismic data and its application in seismic deconvolution. IEEE Trans. Geosci. Rem. Sens. 60, 1-17. https://doi.org/10.1109/TGRS.2021.3076991.
- Gholami, A., Sacchi, M.D., 2012. A fast and automatic sparse deconvolution in the presence of outliers. IEEE Trans. Geosci. Rem. Sens. 50, 4105-4116. https:// doi.org/10.1109/TGRS.2012.2189777.
- Goodfellow, I.J., Pouget-Abadie, J., Mirza, M., Xu, B., Warde-Farley, D., Ozair, S., Courville, A., Bengio, Y., 2014. Generative adversarial nets. In: Proceedings of the 27th International Conference on Neural Information Processing Systems -Volume 2. MIT Press, Cambridge, MA, USA, pp. 2672-2680.
- Grady, T.J., Khan, R., Louboutin, M., Yin, Z., Witte, P.A., Chandra, R., Hewett, R.J., Herrmann, F.J., 2023. Model-parallel Fourier neural operators as learned surrogates for large-scale parametric PDEs. Comput. Geosci. 178, 105402. https:// doi.org/10.1016/j.cageo.2023.105402.
- Guo, A.H., Lu, P.F., Wang, D.D., Wu, J.Z., Xiao, C., Peng, H.Y., Jiang, S.H., 2023. Improving the resolution of poststack seismic data based on UNet+GRU deep learning method. Appl. Geophys. 20, 1-10. https://doi.org/10.1007/s11770-023-
- Hale, D., 1981. An inverse Q-filter. Stanford Exploration Project Report 26, 231-243. Hamida, A., Alfarraj, M., Al-Shuhail, A.A., Zummo, S.A., 2023. Facies-guided seismic image super-resolution. IEEE Trans. Geosci. Rem. Sens. 61, 1-13. https://doi.org/ 10.1109/TGRS.2023.3289151.
- Hargreaves, N.D., Calvert, A.J., 1991. Inverse Q filtering by fourier transform. Geophysics 56, 519-527. https://doi.org/10.1190/1.1443067
- Harsuko, R., Alkhalifah, T.A., 2022. Storseismic: a new paradigm in deep learning for seismic processing, IEEE Trans. Geosci. Rem. Sens. 60, 1-15. https://doi.org/ 10.1109/TGRS.2022.3216660.
- Ho, J., Jain, A., Abbeel, P., 2020. Denoising diffusion probabilistic models. In: Larochelle, H., Ranzato, M., Hadsell, R., Balcan, M., Lin, H. (Eds.), Advances in Neural Information Processing Systems. Curran Associates, Inc., pp. 6840-6851
- Hou, S., Wang, C., Zeng, Q., Cui, D., Yan, Y., Zhang, C., Zhang, Z., 2023. Seismic data interpolation based on diffusion model deep learning. In: Third International Meeting for Applied Geoscience & Energy Expanded Abstracts, pp. 1588–1592. https://doi.org/10.1190/image2023-3915640.1.
- Huang, N.E., Shen, Z., Long, S.R., Wu, M.C., Shih, H.H., Zheng, Q., Yen, N.C., Tung, C.C., Liu, H.H., 1998. The empirical mode decomposition and the Hilbert spectrum for nonlinear and non-stationary time series analysis. Proc. Royal Soci. London. Series A: Math. Phys. Eng. Sci. 454, 903-995. https://doi.org/10.1098/ rspa.1998.0193.
- Jiang, F., Osypov, K., Toms, J., 2023. Implementation of denoising diffusion probability model for seismic interpretation. In: Third International Meeting for Applied Geoscience & Energy Expanded Abstracts, pp. 1098-1102. https:// doi.org/10.1190/image2023-3907375.1
- Jiang, Y., Cao, S., Chen, S., Zheng, D., 2021. A blind nonstationary deconvolution method for multichannel seismic data. Explor. Geophys. 52, 245-257. https:// doi.org/10.1080/08123985.2020.1807319.
- Kazemi, N., Sacchi, M.D., 2014. Sparse multichannel blind deconvolution. Geophysics 79, V143-V152. https://doi.org/10.1190/geo2013-0465.1.
- Kjartansson, E., 1979. Constant Q-wave propagation and attenuation. J. Geophys. Res. Solid Earth 84, 4737–4748, https://doi.org/10.1029/IB084iB09p04737.
- Kullback, S., Leibler, R.A., 1951. On information and sufficiency. Ann. Math. Stat. 22, 79-86. https://doi.org/10.1214/aoms/1177729694.

Leinbach, J., 1995. Wiener spiking deconvolution and minimum-phase wavelets: a tutorial. Lead. Edge 14, 189–192. https://doi.org/10.1190/1.1437110.

- Levin, S.A., 1989. Surface-consistent deconvolution. Geophysics 54, 1123–1133. https://doi.org/10.1190/1.1442747.
- Levy, S., Fullagar, P.K., 1981. Reconstruction of a sparse spike train from a portion of its spectrum and application to high-resolution deconvolution. Geophysics 46, 1235—1243. https://doi.org/10.1190/1.1441261.
- Li, G., Liu, Y., Zheng, H., Huang, W., 2015. Absorption decomposition and compensation via a two-step scheme. Geophysics 80, V145–V155. https://doi.org/10.1190/geo2015-0038.1.
- Li, H., Li, G.F., Ma, X., Zhang, J.L., Meng, Q.L., Zhang, Z.X., 2021. Multichannel deconvolution with spatial reflection regularization. Appl. Geophys. 18, 85–93. https://doi.org/10.1007/s11770-021-0852-z.
- Li, J., Wu, X., Hu, Z., 2022. Deep learning for simultaneous seismic image superresolution and denoising. IEEE Trans. Geosci. Rem. Sens. 60, 1–11. https:// doi.org/10.1109/TGRS.2021.3057857.
- Li, Y., Alkhalifah, T., Huang, J., Li, Z., 2023. Self-supervised pretraining vision transformer with masked autoencoders for building subsurface model. IEEE Trans. Geosci. Rem. Sens. 61, 1–10. https://doi.org/10.1109/TGRS.2023.3308999.
- Lin, L., Zhong, Z., Cai, C., Li, C., Zhang, H., 2023. SeisGAN: improving seismic smage resolution and reducing random noise using a generative adversarial network. Math. Geosci. https://doi.org/10.1007/s11004-023-10103-8.
- Lin, Y., Chen, S., Zhang, G., Huang, M., Wang, B., 2022. High-resolution time—frequency analysis based on a synchroextracting adaptive S-transform and its application. J. Geophys. Eng. 19, 1124—1133. https://doi.org/10.1093/jge/gxac068.
- Liu, D., Niu, W., Wang, X., Sacchi, M.D., Chen, W., Wang, C., 2023a. Improving vertical resolution of vintage seismic data by a weakly supervised method based on cycle generative adversarial network. Geophysics 88, V445–V458. https:// doi.org/10.1190/geo2023-0006.1.
- Liu, Q., Ma, J., 2024. Generative interpolation via a diffusion probabilistic model. Geophysics 89, V65–V85. https://doi.org/10.1190/geo2023-0182.1.
- Liu, S., Birnie, C., Alkhalifah, T., 2023b. Trace-wise coherent noise suppression via a self-supervised blind-trace deep-learning scheme. Geophysics 88, V459—V472. https://doi.org/10.1190/geo2022-0371.1.
- Luo, C., 2022. Understanding diffusion models: A unified perspective. arXiv: 2208.11970.
- Ma, M., Wang, S., Yuan, S., Wang, J., Wen, J., 2017. Multichannel spatially correlated reflectivity inversion using block sparse Bayesian learning. Geophysics 82, V191–V199. https://doi.org/10.1190/geo2016-0366.1.
- Margrave, G.F., 1998. Theory of nonstationary linear filtering in the fourier domain with application to time-variant filtering. Geophysics 63, 244–259. https://doi.org/10.1190/1.1444318.
- Margrave, G.F., Lamoureux, M.P., Henley, D.C., 2011. Gabor deconvolution: estimating reflectivity by nonstationary deconvolution of seismic data. Geophysics 76, W15—W30. https://doi.org/10.1190/1.3560167.
- Min, F., Wang, L., Pan, S., Song, G., 2023. D<sup>2</sup>UNet: dual decoder U-Net for seismic image super-resolution reconstruction. IEEE Trans. Geosci. Rem. Sens. 61, 1–13. https://doi.org/10.1109/TGRS.2023.3264459.
- Oliveira, D.A.B., Ferreira, R.S., Silva, R., Brazil, E.V., 2019. Improving seismic data resolution with deep generative networks. Geosci. Rem. Sens. Lett. IEEE 16, 1929–1933. https://doi.org/10.1109/LGRS.2019.2913593.
- Oropeza, V., Sacchi, M., 2011. Simultaneous seismic data denoising and reconstruction via multichannel singular spectrum analysis. Geophysics 76, V25–V32. https://doi.org/10.1190/1.3552706.
- Pan, Z., Yu, W., Wang, B., Xie, H., Sheng, V.S., Lei, J., Kwong, S., 2020. Loss functions of generative adversarial networks (GANs): opportunities and challenges. IEEE Transact. Emerg. Topics Computat. Intellig. 4, 500–522. https://doi.org/10.1109/ TETCI.2020.2991774.
- Peacock, K.L., Treitel, S., 1969. Predictive deconvolution: theory and practice. Geophysics 34, 155–169. https://doi.org/10.1190/1.1440003.
- Peng, J., Li, Y., Liao, Z., Wang, X., Yang, X., 2024. Seismic data strong noise attenuation based on diffusion model and principal component analysis. IEEE Trans. Geosci. Rem. Sens. 62, 1–11. https://doi.org/10.1109/TGRS.2024.3355460.
- Puryear, C.I., Castagna, J.P., 2008. Layer-thickness determination and stratigraphic interpretation using spectral inversion: theory and application. Geophysics 73, R37–R48. https://doi.org/10.1190/1.2838274.
- Robinson, E.A., 1967. Predictive decomposition of time series with application to seismic exploration. Geophysics 32, 418–484. https://doi.org/10.1190/1.1439873.
- Ronneberger, O., Fischer, P., Brox, T., 2015. U-Net: convolutional networks for biomedical image segmentation. In: Navab, N., Hornegger, J., Wells, W.M., Frangi, A.F. (Eds.), Medical Image Computing and Computer-Assisted Intervention – MICCAI 2015. Springer International Publishing, Cham, pp. 234—241.
- Sacchi, M.D., 1997. Reweighting strategies in seismic deconvolution. Geophys. J. Int. 129, 651–656. https://doi.org/10.1111/j.1365-246X.1997.tb04500.x.
- Saharia, C., Chan, W., Chang, H., Lee, C., Ho, J., Salimans, T., Fleet, D., Norouzi, M., 2022. Palette: image-to-image diffusion models. In: ACM SIGGRAPH 2022 Conference Proceedings. Association for Computing Machinery, New York, NY, USA. https://doi.org/10.1145/3528233.3530757.
- Saharia, C., Ho, J., Chan, W., Salimans, T., Fleet, D.J., Norouzi, M., 2023. Image superresolution via iterative refinement. IEEE Trans. Pattern Anal. Mach. Intell. 45, 4713–4726. https://doi.org/10.1109/TPAMI.2022.3204461.
- Sohn, K., Lee, H., Yan, X., 2015. Learning structured output representation using deep conditional generative models. In: Cortes, C., Lawrence, N., Lee, D.,

Sugiyama, M., Garnett, R. (Eds.), Advances in Neural Information Processing Systems, Curran Associates, Inc.

- Song, C., Wang, Y., 2022. High-frequency wavefield extrapolation using the Fourier neural operator. J. Geophys. Eng. 19, 269–282. https://doi.org/10.1093/jge/gxac016
- Song, J., Meng, C., Ermon, S., 2021a. Denoising diffusion implicit models. In: International Conference on Learning Representations.
- Song, Y., Sohl-Dickstein, J., Kingma, D.P., Kumar, A., Ermon, S., Poole, B., 2021b. Score-based generative modeling through stochastic differential equations. In: International Conference on Learning Representations.
- Stockwell, R., Mansinha, L., Lowe, R., 1996. Localization of the complex spectrum: the S transform. IEEE Trans. Signal Process. 44, 998–1001. https://doi.org/10.1109/78.492555.
- Sun, H., Demanet, L., 2020. Extrapolated full-waveform inversion with deep learning. Geophysics 85, R275–R288. https://doi.org/10.1190/geo2019-0195.1.
- Sun, Q.F., Xu, J.Y., Zhang, H.X., Duan, Y.X., Sun, Y.K., 2022. Random noise suppression and super-resolution reconstruction algorithm of seismic profile based on GAN. J. Pet. Explor. Prod. Technol. 12, 2107–2119. https://doi.org/10.1007/s13202-021-01447-0.
- Sun, Y., Liu, Y., Dong, H., Chen, G., Li, X., 2024. Seismic AVO inversion method for viscoelastic media based on a tandem invertible neural network model. IEEE Trans. Geosci. Rem. Sens. 62, 1–18. https://doi.org/10.1109/TGRS.2024.3355481.
- Sun, Y.H., Liu, Y., 2022. Model-data-driven P-wave impedance inversion using ResNets and the normalized zero-lag cross-correlation objective function. Petrol. Sci. 19, 2711–2719. https://doi.org/10.1016/j.petsci.2022.09.008.
- Petrol. Sci. 19, 2711–2719. https://doi.org/10.1016/j.petsci.2022.09.008. Taylor, H.L., Banks, S.C., McCoy, J.F., 1979. Deconvolution with the  $L_1$  norm. Geophysics 44, 39–52. https://doi.org/10.1190/1.1440921.
- Velis, D.R., 2008. Stochastic sparse-spike deconvolution. Geophysics 73, R1—R9. https://doi.org/10.1190/1.2790584.
- Wang, F., Huang, X., Alkhalifah, T.A., 2023a. A prior regularized full waveform inversion using generative diffusion models. IEEE Trans. Geosci. Rem. Sens. 61, 1–11. https://doi.org/10.1109/TGRS.2023.3337014.
- Wang, L., Gao, J., Zhao, W., Jiang, X., 2013. Enhancing resolution of nonstationary seismic data by molecular-Gabor transform. Geophysics 78, V31–V41. https:// doi.org/10.1190/geo2011-0450.1.
- Wang, Y., 2002. A stable and efficient approach of inverse Q filtering. Geophysics 67, 657–663. https://doi.org/10.1190/1.1468627.
- Wang, Y., 2006. Inverse Q-filter for seismic resolution enhancement. Geophysics 71, V51–V60. https://doi.org/10.1190/1.2192912.
- Wang, Y., Xu, J., Zhao, Z., Gao, Y., Zhang, H., 2024. Structurally-constrained unsupervised deep learning for seismic high-resolution reconstruction. IEEE Trans. Geosci. Rem. Sens. 62, 5901115. https://doi.org/10.1109/TGRS.2023.3340888.
- Wang, Z., Zheng, H., He, P., Chen, W., Zhou, M., 2023c. Diffusion-GAN: training GANs with diffusion. In: The Eleventh International Conference on Learning Representations.
- Wei, X., Zhang, C., Wang, H., Tan, C., Xiong, D., Jiang, B., Zhang, J., Kim, S.W., 2023. Seismic data interpolation based on denoising diffusion implicit models with resampling. arXiv:2307.04226.
- Wu, X., Geng, Z., Shi, Y., Pham, N., Fomel, S., Caumon, G., 2020. Building realistic structure models to train convolutional neural networks for seismic structural interpretation. Geophysics 85, WA27—WA39. https://doi.org/10.1190/geo2019-0275.1
- Wu, X., Liang, L., Shi, Y., Fomel, S., 2019. FaultSeg3D: using synthetic data sets to train an end-to-end convolutional neural network for 3D seismic fault segmentation. Geophysics 84, IM35-IM45. https://doi.org/10.1190/geo2018-0646.1.
- Xu, L., Gao, Z., Hu, S., Gao, J., Xu, Z., 2022. Simultaneous inversion for reflectivity and Q using nonstationary seismic data with deep-learning-based decoupling. IEEE Trans. Geosci. Rem. Sens. 60, 1–15. https://doi.org/10.1109/TGRS.2022.3226723.
- Yang, L., Zhang, Z., Song, Y., Hong, S., Xu, R., Zhao, Y., Zhang, W., Cui, B., Yang, M.H., 2023a. Diffusion models: a comprehensive survey of methods and applications. ACM Comput. Surv. 56, 1–39. https://doi.org/10.1145/3626235.
- Yang, N.X., Li, G.F., Li, T.H., Zhao, D.F., Gu, W.W., 2024. An improved deep dilated convolutional neural network for seismic facies interpretation. Petrol. Sci. 21, 1569–1583. https://doi.org/10.1016/j.petsci.2023.11.027.
- Yang, S., Alkhalifah, T., Ren, Y., Liu, B., Li, Y., Jiang, P., 2023b. Well-log information-assisted high-resolution waveform inversion based on deep learning. Geosci. Rem. Sens. Lett. IEEE 20, 1–5. https://doi.org/10.1109/LGRS.2023.3234211.
- Yao, Z., Gao, X., Li, W., 2003. The forward Q method for compensating attenuation and frequency dispersion used in the seismic profile of depth domain. Chin. J. Geophys. 46, 229–233 (in Chinese).
- Yilmaz, 2001. Seismic Data Analysis. Society of Exploration Geophysicists.
- Zeng, D., Xu, Q., Pan, S., Song, G., Min, F., 2023. Seismic image super-resolution reconstruction through deep feature mining network. Appl. Intell. 53, 21875–21890. https://doi.org/10.1007/s10489-023-04660-y.
- Zhang, C., Ulrych, T.J., 2007. Seismic absorption compensation: a least squares inverse scheme. Geophysics 72, R109—R114. https://doi.org/10.1190/1.2766467.
- Zhang, G.L., Lin, J., Wand, X.M., He, Z.H., Cao, J.X., Zhang, J.J., He, X.L., Lin, K., Xue, Y.J., 2015. A self-adaptive approach for inverse Q-filtering. Chin. J. Geophys. 58, 2525–2535. https://doi.org/10.6038/cjg20150727 (in Chinese).
- Zhang, H., Alkhalifah, T., Liu, Y., Birnie, C., Di, X., 2023. Improving the generalization of deep neural networks in seismic resolution enhancement. Geosci. Rem. Sens. Lett. IEEE 20, 1–5. https://doi.org/10.1109/LGRS.2022.3229167.
- Zhang, H., Chen, T., Liu, Y., Zhang, Y., Liu, J., 2021. Automatic seismic facies interpretation using supervised deep learning. Geophysics 86, IM15—IM33. https://

## doi.org/10.1190/geo2019-0425.1.

- Zhang, H., Wang, W., Wang, X., Chen, W., Zhou, Y., Wang, C., Zhao, Z., 2019a. An implementation of the seismic resolution enhancing network based on GAN. In: SEG Technical Program Expanded Abstracts 2019, pp. 2478–2482. https://doi.org/10.1190/segam2019-3216229.1.
- Zhang, H., Yang, P., Liu, Y., Luo, Y., Xu, J., 2022a. Deep learning-based low-frequency extrapolation and impedance inversion of seismic data. Geosci. Rem. Sens. Lett. IEEE 19, 1–5. https://doi.org/10.1109/LGRS.2021.3123955.
- Zhang, M., Liu, Y., 2022. 3-D seismic data recovery via neural network-based matrix completion. Geosci. Rem. Sens. Lett. IEEE 19, 1–5. https://doi.org/10.1109/LGRS.2022.3154816.
- Zhang, M., Liu, Y., Bai, M., Chen, Y., 2019b. Seismic noise attenuation using
- unsupervised sparse feature learning. IEEE Trans. Geosci. Rem. Sens. 57, 9709–9723, https://doi.org/10.1109/TGRS.2019.2928715.
- Zhang, R., Castagna, J., 2011. Seismic sparse-layer reflectivity inversion using basis pursuit decomposition. Geophysics 76, R147–R158. https://doi.org/10.1190/ geo2011-0103.1.
- Zhang, S.B., Si, H.J., Wu, X.M., Yan, S.S., 2022b. A comparison of deep learning methods for seismic impedance inversion. Petrol. Sci. 19, 1019–1030. https:// doi.org/10.1016/j.petsci.2022.01.013.
- Zhou, H.L., Wang, J., Wang, M.C., Shen, M.C., Zhang, X.K., Liang, P., 2014. Amplitude spectrum compensation and phase spectrum correction of seismic data based on the generalized S transform. Appl. Geophys. 11,. https://doi.org/10.1007/s11770-014-0456-y, 468-478+510-511.